Mixed-numerology Signals Transmission and Interference Cancellation for Radio Access Network Slicing

Bowen Yang, Lei Zhang, Oluwakayode Onireti, Pei Xiao, Muhammad Ali Imran and Rahim Tafazolli

***Abstract*—A clear understanding of mixed-numerology signals multiplexing and isolation in the physical layer is of importance to enable spectrum efficient radio access network (RAN) slicing, where the available access resource is divided into slices to cater to services/users with optimal individual design. In this paper, a RAN slicing framework is proposed and systematically analyzed from a physical layer perspective. According to the baseband and radio frequency (RF) configurations imparities among slices, we categorize four scenarios and elaborate on the numerology relationships of slices configurations. By considering the most generic scenario, system models are established for both uplink and downlink transmissions. Besides, a low out of band emission (OoBE) waveform is implemented in the system for the sake of signal isolation and inter-service/slice-band-interference (ISBI) mitigation. We propose two theorems as the basis of algorithms design in the established system, which generalize the original circular convolution property of discrete Fourier transform (DFT). Moreover, ISBI cancellation algorithms are proposed based on a collaboration detection scheme, where joint slices signal models are implemented. The framework proposed in the paper establishes a foundation to underpin extremely diverse user cases in 5G that implement on a common infrastructure.**

***Index Terms*—radio access network slicing (RAN slicing), generalized circular convolution property, inter-service/slice-band-interference (ISBI), multi-service, multi/mixed-numerology**

I. Introduction

THE fifth generation (5G) wireless network and beyond is supposed to facilitate a fully mobile and connected community, where a variety of use cases with very diverse requirements in terms of throughput, latency, reliability and scalability will be supported concurrently [1]. Based on the unique features and technical requirements of different services, three main use cases have been identified for 5G, i.e., enhanced mobile broadband (eMBB), massive machine-type communications (mMTC), and ultra-reliable low latency communications (URLLC) [1], [2]. As a solution to support all scenarios, network slicing enables design, deployment, customization, and optimization of different network slices on *a common infrastructure* [3]–[5]. Recent researches on network slicing focus on the core network to provide dedicated virtual networks [3], [6], [7]. From the physical layer perspective, due to the extremely diverse requirements among services and use cases, the service configurations in different resource slices[1] may be significantly different [2], [8], [9]. These imparities could be in either baseband (BB) (e.g., frame structure, subcarrier spacing, etc.) and/or in radio frequency (RF) front-end (e.g., processing bandwidth or sampling rate, etc.). For example, mMTC service might require a slice with small subcarrier spacing (and thus larger symbol duration) to support massive delay-tolerant devices and also enable its power-boosting gain in some extreme cases [10]. On the other hand, vehicle to vehicle (V2V) communications has much more stringent latency and reliability requirements [11], which necessitates significantly smaller symbol duration compared with the mMTC scenario. Moreover, for the high data rate eMBB communications, the subcarrier spacing and symbol duration can not go to extreme values due to the channel doubly dispersion constraints. Meanwhile, the limitation on cost, complexity and energy consumption of the communication devices may also affect the physical layer configurations. In particular, the RF bandwidth of the RF filter and digital to analog (D/A, or A/D) converter of a low-end MTC device could be significantly smaller than the full system bandwidth as compared to the normal user equipment (UE) or base station (BS) [12].

To support such a heterogeneous mixed-numerology or multi-numerology system[2] with physical layer configuration imparity among slices on a common infrastructure (i.e., BS), the transceiver architecture and widely used algorithms in the traditional single-service system may need to be significantly changed. One change of paramount importance is how to keep the low complexity and effective one-tap channel equalization (and estimation). In a single-service multicarrier system, it is known that such an equalizer is validated by the original circular convolution property of discrete Fourier transform (O-CCP-DFT), which diagonalizes the channel matrix and contributes to flat fading sub-channels [13]. Long term evolution (LTE) is such kind of system where all users share the same RF and BB configurations. However, the O-CCP-DFT in mixed-numerology systems may be invalidated because the mismatched sampling rate between transmitter and receiver could result in a misaligned DFT/IDFT processing pair. To underpin the system algorithms design, a generalized CCP-DFT (G-CCP-DFT) is proposed and theoretically investigated.

This work was supported by U.K. EPSRC project EP/S02476X/1. (*Corresponding author: Lei Zhang*.)

Bowen Yang, Lei Zhang, Oluwakayode Onireti, and Muhammad Ali Imran are with James Watt School of Engineering, University of Glasgow, Glasgow, G12 8QQ, UK. Pei Xiao and Rahim Tafazolli are with the 5G Innovation Centre (5GIC), University of Surrey, Guildford, GU2 7XH, UK. (Email: b.yang.1@research.gla.ac.uk; lei.zhang@glasgow.ac.uk; oluwakayode.onireti@glasgow.ac.uk; p.xiao@surrey.ac.uk; muhammad.imran@glasgow.ac.uk; r.tafazolli@surrey.ac.uk).

[1]It is worth noting that in this case, resource slice is also called bandwidth part in the 3rd Generation Partnership Project (3GPP) 5G standardization.

[2]One should note that in this paper, the term 'numerology' denotes the unique physical layer configurations associated with a dedicated slice, where not only subcarrier spacing but also other RF and baseband configurations are taken into account.

Another key challenge associated with the RAN slicing in the physical layer is the mixed-numerology signals multiplexing and isolation. In principle, slices can be multiplexed in any orthogonal access resources from either time or frequency domain [8], or be multiplexed with shared resources [14], [15]. Compared with the time division multiplexing (TDM), frequency division multiplexing (FDM) has several advantages such as better forward compatibility, ease of supporting services with different latency requirements, energy saving by turning off the BS transceiver chain for some transmit time intervals (TTIs), etc [16], [17]. In addition, FDM can support finer slices or scheduling granularity (e.g., Internet of Things (IoT)) and thus achieve more flexible and spectrum efficient RAN slicing. However, combining multiple services/slices with different physical layer configurations into one baseband in FDM is more challenging than in TDM due to the loss of orthogonality between slices, and will result in inter-service-band-interference (ISBI)[3] [8]. For these reasons, in this paper, we will focus on the FDM based RAN slicing systems and tackle the corresponding challenges.

To guarantee a satisfactory performance in FDM based RAN slicing systems, confining the signal within its assigned subband and minimize ISBI is the key. In theory, the ISBI level depends on 1) the BB and RF configuration differences among slices, 2) the guardband between service bands, 3) the transceiver processing procedures and 4) the implemented algorithms, etc. For instance, larger guardband or smaller configuration imparity among slices can reduce the interference level. Additionally, waveform plays an essential role in determining the interference level. Many waveforms have been proposed in the literature to reduce the signal out of band emission (OoBE), among which subcarrier filtered multicarrier system and subband filtered multicarrier (SFMC) system are the two most widely used classes. The former includes filter-bank multi-carrier (FBMC) [19] and generalized frequency division multiplexing (GFDM) [20], while the latter includes universal filtered multi-carrier (UFMC) [8], [21], [22], filtered orthogonal frequency division multiplexing (F-OFDM) [23] and windowed OFDM (W-OFDM) [24]. In this paper, we consider F-OFDM to achieve better signal isolation due to its excellent trade-off between performance and complexity [16], [25], as well as the flexibility it can provide for the subband configurations [26]. However, the results can be extended by using other waveforms.

Considering the aforementioned issues and challenges, a framework model that takes the BB and RF differences and the low OoBE waveform into account is of importance for 5G and beyond multi-service systems in terms of parameter selection, algorithm and frame structure design, etc. In addition, with different physical layer configurations among slices, the widely used algorithms and signal processing procedures might be fundamentally affected, such as channel equalization/estimation, random access and synchronization, etc. Note that some of the current researches on RAN slicing focus on the MAC layer scheduling [27], [28], which is different from the work investigated in this paper. In general, RAN slicing on MAC layer scheduling need to consider to aggregate multiple radio access technologies (RATs) (e.g., 802.11 and LTE, etc.) in a common infrastructure to achieve the maximum flexibility and availability. From the physical layer perspective, however, different RATs' signals are well isolated due to the fairly separated frequency bands and RF filters. Thus, the main challenge of RAN slicing on MAC layer scheduling is invisible to the physical layer.

There have been some studies in the literature on mixed-numerology signals multiplexing and isolation. By considering baseband numerology imparity only, [8] proposed a comprehensive framework for the mixed-numerology system to support multiple types of slices each having individual optimized subcarrier spacing. The system model, ISBI cancellation algorithms and framework performance analysis were presented for downlink transmission. The authors in [18] performed a thorough investigation of INI based on the CP-OFDM waveform, where critical factors that affect the power of INI are analyzed, and INI mitigation techniques are discussed. In [29], INI-aware scheduling methods are proposed for the purpose to enhance the reliability in the multi-numerology systems, by which no additional spectral usage, computational complexity, and latency will be caused. In [30], a multi-service system called flexible configured OFDM (FC-OFDM) that utilizes time domain windowing to reduce the system OoBE was proposed. The authors in [30] also proposed a novel low-complexity (with two taps only) precoding scheme in order to mitigate the interference. In addition, [31] proposed a mixed-numerology system based on the FBMC waveform that provides better OoBE and isolation between service bands. In terms of the RF configuration imparity, In-band and Guard-band Narrow-band IoT (NB-IoT) is a special and practical case for the RAN slicing study, and it has been adopted as a feature of the LTE-Advanced Pro [10]. Low cost NB-IoT devices operating at a much lower sampling rate (e.g., 240 kHz [32]) are multiplexed with the normal LTE UEs (with sampling rate 30.72 MHz) on the same infrastructure (i.e., BS). A recent paper [33] proposed a channel equalization algorithm and interference analysis for the uplink of an NB-IoT based OFDM system. The contributions and novelties of this paper are summarized as follows:

- The generalized circular convolution properties of DFT are specified into two theorems by considering upsampling and downsampling, respectively. These theorems provide the theoretical foundation for the advanced interference analysis and cancellation algorithms in both uplink and downlink of the proposed system model.
- We build a comprehensive RAN slicing framework based on practical 5G scenarios and use cases, within which four scenarios are categorized by considering the configurations imparities in both BB and RF.
  The uplink and downlink system models for the most generic scenario, i.e., DBDR, are derived.
- We systematically derive the relationships among most of the key physical layer parameters, including subcarrier spacing, symbol duration, sampling rate, DFT size and waveforms for different scenarios, which constitutes the numerology framework for the proposed systems. We later use this as the basis for our algorithms and system design.

[3]The term ISBI is used in this paper to keep consistency with our previous work [8]. However, it should be noted that in other works like [14] [15] and [18], the term inter-numerology-interference (INI) is used instead to denote the interference between slices.

TABLE I
LIST OF IMPORTANT SYMBOLS

Symbol	*Meaning*	*Symbol*	*Meaning*
Δf	Subcarrier spacing	L	The length of transmit symbol
S	RF processing bandwidth or Sampling rate	η	The value of shifted phase
B	System bandwidth	$\mathbf{\Phi}/\mathbf{\Psi}$	Phase shift matrices
M	Number of subcarriers in a slice band	$\mathbf{U}_Q/\mathbf{D}_Q$	Up-sampling and down-sampling matrices
Q	Sampling mismatch rate	$\mathbf{h}/\mathbf{H}$	Channel impulse response and frequency response
G	Subcarrier spacing mismatch rate	$\mathbf{B}$	Toeplitz channel matrix
ΔT	Symbol duration	$\mathbf{g}/\mathbf{G}$	Filter impulse response and frequency response
N	DFT size	$\mathbf{A}$	Toeplitz filter matrix
L_{CP}	The length of CP	$\mathbf{C}/\mathbf{R}$	CP insertion and removal matrices

* Subscripts that are used to denote different numerologies are omitted due to the limited space. For the same reason, all superscripts are excluded.

- We derive the closed-form power pre-compensation algorithms to overcome the frequency selectivity for both uplink and downlink cases. In addition, based on the derived overall signal collaboration model, low complexity but effective ISBI cancellation algorithms for SBDR cases are proposed by either joint detection in the uplink or precoding in the downlink.

Notations: $\{\cdot\}^H$ and $\{\cdot\}^T$ stand for the Hermitian conjugate and transpose operation, respectively. We use $\mathbb{E}\{\mathbf{A}\}$ and $\text{diag}\{\mathbf{A}\}$ to denote the expectation of matrix $\mathbf{A}$ and a diagonal matrix formed by taking the diagonal elements of $\mathbf{A}$, respectively. $\text{diag}\{\mathbf{a}\}$ denotes forming a diagonal matrix $\mathbf{A}$ using the vector $\mathbf{a}$. $\mathbf{I}_M$ and $\mathbf{0}_{M\times N}$ denote an M-dimensional identity matrix and an $M \times N$ zero matrix, respectively. In addition, we use $\mathbf{F}_N$ to express the N-point power normalized inverse DFT matrix with its i-th row and k-th column being $\frac{1}{\sqrt{N}}e^{j2\pi ik/N}$. The operator $*$ refers to linear convolution. $\text{mod}(a, b)$ means modulo operation and $|\mathbf{A}|^n$ refers to the n-th power of absolute values of all elements in matrix $\mathbf{A}$. To reuse the symbols, we will use $\{\bar{\cdot}\}$ and $\{\hat{\cdot}\}$ to represent the symbols that are related to the uplink and downlink transmissions, respectively. In addition, the commonly used symbols and their meanings are listed in Table I for ease of reference. Note that symbol subscripts to denote different numerologies are omitted in the table due to the limited space. However, explicit symbols' meanings can be found in the paper, e.g., Δf_1 means the subcarrier spacing of slice 1. All superscripts have also been excluded in Table I for the same reason.

II. PHYSICAL-LAYER RADIO ACCESS NETWORK SLICING FRAMEWORK

Consider that a baseband resource is split into subbands and each subband is assigned to one access slice. Each access slice could be shared by multiple users that have the same configurations. This implies that the users do not have to be of the same type but with similar communication requirements, such as data rate, cost, complexity, etc. For example, smart phone and Mobile Virtual Network Operators (MVNO) have similar communication requirements [5]. Hence, they can be assigned to the same slice and their differences are invisible at the physical layer. However, communication scenarios with significantly different requirements, e.g., eMBB and V2V, should be categorized into different slices.

As has been discussed, one of the key challenges for the proposed physical layer slicing system is the mitigation/cancellation of ISBI. It is worth mentioning that a slice can be interfered by more than one neighboring slices above and/or below its allocated subband. Hence, a three-slices (and more) model, e.g., slice1-slice2-slice3, could be considered to present a general case for the interference analysis. However, because the interference generated from each slice is linearly superposed in each victim subband, the model can be decoupled as three simple ones, i.e., slice1-slice2, slice2-slice3 and slice1-slice3. In this paper, without loss of generality, we consider two slices and each slice contains one UE for simplifying the derivation and easy understanding.

A. Four Scenarios of Physical Layer RAN Slicing

We consider four scenarios based on the differences in the slices configurations at BB and RF. For the sake of saving cost, we consider that BS has one single RF chain with fixed bandwidth to process all slices, while each slice could be processed by specific RF chains at each UE who may have different RF configurations. However, at the BS, the baseband configurations could be different among slices. To be specific, the four scenarios are defined in details as follows:

1) SBSR (Slices have the same BB and the same RF configurations): The subcarrier spacing values in the two slices satisfy $\Delta f_1 = \Delta f_2$ and the RF processing bandwidths of the two UEs are equal to the whole system bandwidth, i.e., $S_1 = S_2 = B$. According to the OFDM modulation principle, the two slices can be orthogonally multiplexed without generating any interference. Typical configured LTE/LTE-A is such a kind of single-service or single-numerology system, where all services have the same configurations.

2) DBSR (Slices have different BB but the same RF configurations): In this scenario, the UEs assigned to the two access resource slices have the same RF processing bandwidth, which is also the same as the system bandwidth, i.e., $S_1 = S_2 = B$. However, the baseband numerologies utilized in the two slices are different, i.e., $\Delta f_1 \neq \Delta f_2$. For example, consider that the two slices are used for eMBB and V2V communications, respectively. Due to the short latency requirement, the symbol duration for the V2V communications slice may be significantly smaller than the eMBB service. However, the two UEs may have the same RF configurations.

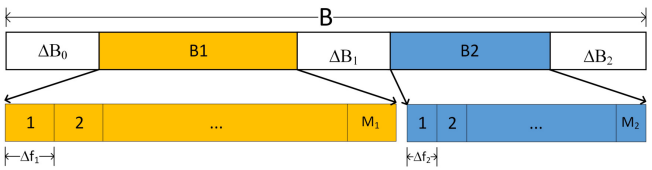

Fig. 1. Spectrum allocation of the two slices within the system bandwidth: $B_1 = M_1\Delta f_1$ for slice 1 and $B_2 = M_2\Delta f_2$ for slice 2.

3) SBDR (Slices have the same BB but different RF configurations): UEs assigned on the two slices have different RF configurations and at least one of them is smaller than the BS sampling rate. Whereas the two slices share the same BB numerology, e.g., $S_1 \neq S_2$, and $\Delta f_1 = \Delta f_2$. A representative example of the scenario is the NB-IoT[4]. Compared with the LTE system configurations of 30.72 MHz sampling rate[5] at both LTE UE and BS, the RF processing bandwidth in NB-IoT UE is significantly smaller (e.g., 240 kHz [32]). The benefits of such design are also significant, as it enables the NB-IoT device to bear only 15% of complexity compared with the legacy LTE UE and contributes to a significant saving of cost and power consumption. In such a scenario, ISBI may be generated since the signal received by the BS is a mixture of narrowband and broadband composite.

4) DBDR (Slices have different BB and different RF configurations): In this scenario, $S_1 \neq S_2$ and $\Delta f_1 \neq \Delta f_2$. DBDR is the most complex scenario. However, it is also the most generic and practical one since it can maximize the potential of RAN slicing by catering for the optimal individual service requirements from both RF and BB perspectives. In the DBDR scenario, the ISBI will be generated from two sources and it could have the worst performance among the four scenarios.

The new communication architecture of the physical layer RAN slicing will significantly affect the existing system design and the algorithms that have been widely used in the single-service system. For example, channel circular convolution property, channel equalization and estimation, and synchronization algorithms may not be applicable in mixed RF configuration scenarios. It is essential to construct a comprehensive framework for the most generic physical RAN slicing scenario (i.e., DBDR) as the foundation of system performance analysis and algorithm design.

B. System Configurations

To build a complete system model, we will first establish the configuration relationships between slices. Specifically, there are at least four key parameters, namely, RF sampling rate, baseband subcarrier spacing (or symbol duration), DFT size (or baseband sampling rate) and waveforms, which may fundamentally affect the system design and performance. In the next, we use $\{\cdot\}_{B1}$, $\{\cdot\}_{B2}$, $\{\cdot\}_{U1}$ and $\{\cdot\}_{U2}$ to denote the parameters associated with the BS for slice 1, BS for slice 2, UE 1 for slice 1 and UE 2 for slice 2, respectively.

Without loss of generality, we assume that the system bandwidth B is normalized, i.e., $B = 1$. As shown in Fig. 1, the bandwidth of slices 1 and 2 are B_1 and B_2, respectively, and ΔB_1 is the guard band in between. We define M_1 and M_2 as the number of subcarriers in the first and second slices, respectively. Besides, ΔB_0 and ΔB_2 are the bandwidth/slices on the left and right of slice 1 and 2, respectively.

1) RF imparity: In principle, the RF bandwidth or sampling rates used in different slices can be arbitrary. However, in practice, it is always beneficial to design a system such that the sampling rate at BS is integer number times that at any UE. For example, in Fig. 2, the sampling rate at the BS is 8 times larger as the sampling rate at UE 2. Without loss of generality, we assume the BS has the same RF configuration as UE 1, and UE 2 is a cost and energy limited device (e.g., IoT device) with $Q \in \mathbb{Z} \geq 1$ times lower sampling rate[6]. The normalized sampling rates can be expressed as

$$S_{B1} = S_{B2} = S_{U1} = B, \quad S_{U2} = \frac{B}{Q} . \tag{1}$$

2) Baseband imparity: Similarly to the RF configuration, it is beneficial to design a physical layer RAN slicing system with an integer least common multiplier (LCM) symbol duration T_{LCM} for all services [8], e.g., as shown in Fig. 2, where slice 1 and 2 symbol duration and subcarrier spacing satisfy the relationship $\Delta T_2 = 2\Delta T_1$ (and $\Delta f_1 = 2\Delta f_2$). In practice, this design principle has been adopted as a basis for the current 5G air interface standardization [17]. For example, assuming the subcarrier spacing for eMBB is 15 kHz, the subcarrier spacing for IoT devices could be selected from the list of 15/8, 15/4, 15/2 kHz, etc. Therefore, we assume that the subcarrier spacing in slice 1 is $G \in \mathbb{Z} \geq 1$ times wider than the one in slice 2, i.e.

$$\Delta f_1 = G\Delta f_2 \; ; \quad \Delta T_2 = G\Delta T_1 \; . \tag{2}$$

From equations (1) and (2), it can be seen that UE 2 has a lower sampling rate, but a larger symbol duration. i.e., both $Q \geq 1$ and $G \geq 1$.

3) DFT/IDFT size and symbol duration in samples: DFT/IDFT size in OFDM based systems depends on the sampling rate and subcarrier spacing. In a physical layer RAN slicing system, its value could be different among slices and also between transmitter and receiver for the same slice due to the RF and/or BB imparities. With the assumptions in this paper, we can have $N_{B1} = S_{B1}/\Delta f_1$ and $N_{B2} = S_{B2}/\Delta f_2$. In addition, by giving equation (1) and that $B_1 = M_1\Delta f_1$ and $B_2 = M_2\Delta f_2$ (as shown in Fig. 1), the DFT sizes for the two slices at the BS are:

$$N_{B1} = \frac{M_1}{B_1}; \; N_{B2} = \frac{M_2}{B_2}. \tag{3}$$

Taking into account the configuration relationships between UE and BS, the DFT sizes of the two UEs could be calculated as:

$$N_{U1} = N_{B1}; \; N_{U2} = \frac{N_{B2}}{Q} \; . \tag{4}$$

N_{B1}, N_{B2}, N_{U1} and N_{U2} can take the values of the integer number power of 2 to facilitate fast Fourier transform (FFT) operation. Equation (4) reveals that UE 1 has the same DFT size as the BS for slice 1 to make the system free of self-interference. However, for slice 2, due to the RF

[4]Note that multi-tone Inband or Guardband NB-IoT [10] is considered here.

[5]Note that such values are only used as examples, the symbols in equations are all normalized and do not correspond to any specific value.

[6]Here we assume $Q \in \mathbb{Z}$, which will facilitate the RF and baseband processing and it aligns with the 3GPP standardization [17].

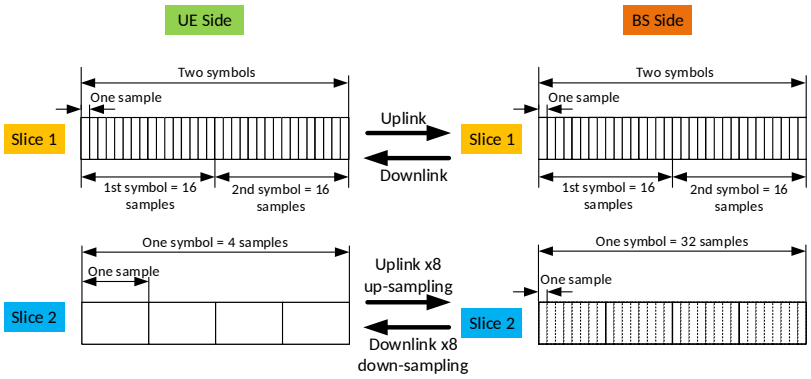

Fig. 2. Frame structure example of DBDR system with two slices:$\Delta T_2 = 2\Delta T_1$ (i.e., $G = 2$ and $\Delta f_1 = 2\Delta f_2$). At UE side, DFT size $N_{U1} = 16$, $N_{U2} = 4$; RF sampling rate $S_{U1} = 8S_{U2}$, (i.e., $Q = 8$). At the BS side, DFT size $N_{B1} = 16$, $N_{B2} = 32$; RF sampling rate $S_{B1} = S_{B2}$ (Note that the two slices are frequency domain multiplexed.).

bandwidth differences between the transmitter and receiver, the DFT/IDFT sizes at BS and UE are different. Specifically, UE 2 can take Q-time smaller DFT than that of the BS.

Let us assume that the CP lengths for slice 1 and slice 2 are $L_{CP,1}$ and $L_{CP,2}$ in the unit of their corresponding UE samples, respectively. With the BS and UE sampling rates relationship in (1), we can equivalently express the CP length for slice 2 as $QL_{CP,2}$ BS samples. By using (2), the symbol duration for the two slices including CP overhead (in the unit of BS samples) can be written as

$$L_1 = N_{B1} + L_{CP,1}\ ; \quad L_2 = N_{B2} + QL_{CP,2}\ . \tag{5}$$

Note that equation (5) is different from (2), where the absolute symbol duration is used. In (5), the symbol duration is expressed as the number of BS samples to facilitate the baseband processing and derivations.

4) Subband filtering waveforms: Due to the multi-numerology between slices and high out of band emission of the OFDM system, the performance of the proposed system may be significantly limited by ISBI, especially the subcarriers located at the edges of the subbands. To reduce the OoBE and mitigate the ISBI, in this paper, we will consider F-OFDM as an example waveform.

Let us denote the subband filter impulse response for the two resource slices at the BS as

$$\begin{aligned} \mathbf{g}_{T1} &= \mathbf{\Psi}_1 \mathbf{g}_{T1,p} \in \mathbb{C}^{N_{B1}\times 1}\ ; \\ \mathbf{g}_{T2} &= \mathbf{\Psi}_2 \mathbf{g}_{T2,p} \in \mathbb{C}^{N_{B2}\times 1}\ , \end{aligned} \tag{6}$$

where $\mathbf{g}_{T1,p}$ and $\mathbf{g}_{T2,p}$ are the prototype filter for slice 1 and 2, respectively[7]. The passband of $\mathbf{g}_{T1,p}$ and $\mathbf{g}_{T2,p}$ are $[0, B_1]$ and $[0, B_2]$, respectively. $\mathbf{\Psi}_1$ and $\mathbf{\Psi}_2$ are diagonal matrices to shift the two prototypes filters to the targeting subbands where the two slices are assigned. The i-th diagonal elements of $\mathbf{\Psi}_1 \in \mathbb{C}^{N_{B1}\times N_{B1}}$ and $\mathbf{\Psi}_2 \in \mathbb{C}^{N_{B2}\times N_{B2}}$ are

$$\Psi_1(i) = e^{j\cdot 2\pi i \eta_1/N_{B_1}}\ ; \quad \Psi_2(i) = e^{j\cdot 2\pi i \eta_2/N_{B_2}}\ , \tag{7}$$

where $\eta_1 = \Delta B_0 N_{B1}$ and $\eta_2 = (\Delta B_0 + \Delta B_1 + B_1)N_{B2}$ are the shifted phase to move the signals to the corresponding frequency subbands. Thus the passband of the two slices' filters $\mathbf{g}_{T1}$ and $\mathbf{g}_{T2}$ are $[\Delta B_0, \Delta B_0 + B_1]$ and $[\Delta B_0 + \Delta B_1 + B_1, \Delta B_0 + \Delta B_1 + B_1 + B_2]$, respectively.

[7]A typical setup for filter length is half DFT size in the F-OFDM system [23]. However, we can always pad zeros at the rear of the filters.

At the UE side, UE 1 can also perform the subband filtering to further reduce the ISBI. However, for UE 2, baseband filtering is not feasible due to the small baseband processing bandwidth. Instead, an RF filter can equivalently take the role of mitigating the interference.

III. Generalized Circular Convolution Properties

One of the paramount advantages of the OFDM system is that it enables low complexity interference free one-tap channel equalization. The rationale is that the original circular convolution property (O-CCP) of DFT [13], where the same size IDFT and DFT pair operating at transmitter and receiver respectively, can diagonalize the channel matrix. This property has been widely adopted in single-service OFDM systems, including 3GPP LTE, IEEE 802.11, etc. However, in the multi-service system, the IDFT and DFT size may be different at the transmitter and receiver, which could invalidate O-CCP. Hence, we propose the generalized circular convolution property (G-CCP) to cater for such new scenarios, who has much more extensive applicability than the original property.

Before we derive G-CCP, let us briefly recall the O-CCP of the DFT processing. According to the **Theorem 4.8.2** in [13], if we define a circular matrix $\mathbf{B} \in \mathbb{C}^{N\times N}$ with its first column being $\mathbf{b} = [b_1, b_2, \cdots, b_N]^T$, and a power normalized IDFT matrix $\mathbf{F}_N \in \mathbb{C}^{N\times N}$. Then we can have $\mathbf{F}_N^H \mathbf{B} \mathbf{F}_N = diag(\lambda_1, \cdots, \lambda_n)$, where $(\lambda_1, \cdots, \lambda_n)$ are the eigenvalues of matrix $\mathbf{B}$. Hence, the circular matrix is diagonalized with paired DFT processing. For the purpose to extend the original property to a generalized form, we consider unpaired DFT processing, which is different from the paired ones in two aspects: 1) the DFT and IDFT sizes are different; 2) the phase between the DFT and IDFT is not aligned. Here, we use 'phase' to denote the state of DFT/IDFT matrix after circulant-shift. For example, the phase of the original DFT matrix is 0. To set its phase to π is equivalent to shift the original matrix circularly by half of the DFT size. To incorporate these two aspects, we define $\mathbf{F}_M \in \mathbb{C}^{M\times M}$ as another power normalized IDFT matrix with $M = N/Q$, and an N-dimensional phase shifting diagonal matrix $\mathbf{\Phi}_\eta$ with its i-th ($i = 0, 1, \cdots, N-1$) diagonal elements being

$$\Phi_\eta(i) = e^{j\cdot 2\pi i \eta/N}\ , \quad \eta \in \mathbb{R} \tag{8}$$

where η indicates the value of the shifted phase. By multiplying $\mathbf{\Phi}_\eta$ and the DFT/IDFT matrix, the phase of the DFT/IDFT

matrix will be shifted by η. In addition, consider the different matrix size of $\mathbf{B}$ and $\mathbf{F_M}$, we introduce an up-sampling matrix $\mathbf{U}_Q \in \mathbb{R}^{N\times M}$ by a factor of Q to enable the multiplication between them. Specifically, $\mathbf{U}_Q$ can be formed as:

$$\mathbf{U}_Q = \begin{pmatrix} \mathbf{1}_u & 0 & \cdots & 0 \\ 0 & \mathbf{1}_u & \cdots & 0 \\ \vdots & \vdots & \ddots & \vdots \\ 0 & 0 & \cdots & \mathbf{1}_u \end{pmatrix}, \tag{9}$$

where $\mathbf{1}_u = [1, 1, \cdots, 1]^T_{1\times Q}$. It should be noted that N and M can be any value in specific cases as long as $N/M = Q$.

Theorem 1 (G-CCP-US): *Let us define $\mathbf{H}_U = \mathbf{F}_N^H \mathbf{B}\mathbf{\Phi}_\eta \mathbf{U}_Q \mathbf{F}_M$, then we have the generalized upsampling circular convolution property of DFT as*

$$\mathbf{H}_U = \mathbf{F}_N^H \mathbf{B}\mathbf{\Phi}_\eta \mathbf{U}_Q \mathbf{F}_M = \frac{1}{\sqrt{Q}} \mathbf{H}_O \mathbf{J}^{(u)} \mathbf{\Upsilon}, \tag{10}$$

where

$$\mathbf{H}_O = \text{diag}(\mathbf{h}_F) = \sqrt{N}\text{diag}(\mathbf{F}_N^H \mathbf{b}) \ , \tag{11}$$

and

$$\mathbf{J}^{(u)} = [\mathbf{I}_{N,1}; \mathbf{I}_{N,2}]. \tag{12}$$

$\mathbf{H}_O$ and $\mathbf{h}_F = \sqrt{N}\mathbf{F}_N^H \mathbf{b}$ are the matrix and vector forms of the N-point DFT of $\mathbf{b}$. $\mathbf{I}_{N,1}$ and $\mathbf{I}_{N,2}$ are obtained by taking the last u and the first $N-u$ rows of identity matrix $\mathbf{I}_N$, where $u = mod(\eta, N)$. $\mathbf{\Upsilon}$ is an $N \times M$-dimension matrix given by $\mathbf{\Upsilon} = [diag(\boldsymbol{\upsilon}_0), diag(\boldsymbol{\upsilon}_1), \cdots,$ $diag(\boldsymbol{\upsilon}_{Q-1})]^T$, with $\boldsymbol{\upsilon}_l$ being Q-length vector and its i-th ($0 \le i \le M-1$) element is obtained as follows

$$\upsilon_l(i) = \frac{1 - e^{j\cdot\frac{2\pi i(Q+lM)}{N}}}{1 - e^{j\cdot\frac{2\pi i(1+lM)}{N}}} \ . \tag{13}$$

Moreover, the power of $\upsilon_l(i)$ can be written as

$$|\upsilon_l(i)|^2 = \Big[\frac{\sin(\frac{\pi i(Q+lM)}{N})}{\sin(\frac{\pi i(1+lM)}{N})}\Big]^2 \ . \tag{14}$$

Proof: See Appendix A. ∎

From the G-CCP-US proposed in Theorem 1 shown in (10), we can see that the matrix $\mathbf{B}$ cannot be diagonalized by the unpaired DFT/IDFT processing and $\mathbf{H}_U$ is with the form where block matrices stacked below each other. In general, if we assume that $mod(\mu, M) = 0$, such block matrices are all diagonal matrices. However, when the constraint $mod(\mu, M) = 0$ cannot hold, each block matrix in $\mathbf{H}_U$ is shifted according to the value of $mod(\mu, M)$. Moreover, the elements of $\mathbf{H}_U$ are weighted by $\mathbf{\Upsilon}$ in a point-wise sense. Although $\mathbf{H}_U$ has a stacked form, it can be transformed into a diagonal matrix with some matrix exchange operations, as shown in (16) and (17). This is also the reason why the proposed Theorem is called generalized circular convolution property. When the up-sampling rate $Q = 1$ and phase shifter $\eta = 0$, Theorem 1 reduces to the O-CCP [13].

One of the applications of G-CCP-US is in telecommunication. Consider a complete multicarrier communication system where the transmitter sampling rate is $1/Q$ that of the receiver's, and $\mathbf{B}$ is the channel matrix and $\mathbf{\Phi}_\eta$ is applied to shift the signal to the allocated subcarriers. By defining $\mathbf{a}_M \in \mathbb{C}^{M\times 1}$ as the transmit signal that is assigned to M consecutive subcarriers (indicated by $m \in [\eta, \eta+1, \cdots, \eta+M-1]$), the received signal can be written as:

$$\mathbf{y}_U = \mathbf{F}_N^H \mathbf{B}\mathbf{\Phi}_\eta \mathbf{U}_Q \mathbf{F}_M = \frac{1}{\sqrt{Q}} \mathbf{H}_O \mathbf{J}^{(u)} \mathbf{\Upsilon} \mathbf{a}_M \ , \tag{15}$$

By using simple matrix exchange operation, (15) can be equivalently written as the following form

$$\mathbf{y}_U = \tilde{\mathbf{H}}_U \tilde{\mathbf{a}}_M \ , \tag{16}$$

where $\tilde{\mathbf{H}}_U = \frac{1}{\sqrt{Q}} \mathbf{H}_O \tilde{\mathbf{\Upsilon}}$ and

$$\tilde{\mathbf{\Upsilon}} = \text{diag}(\mathbf{J}^{(u)}[\boldsymbol{\upsilon}_0, \boldsymbol{\upsilon}_1, \cdots, \boldsymbol{\upsilon}_{Q-1}]^T) \ . \tag{17}$$

$\tilde{\mathbf{a}}_M = \mathbf{J}^{(u)}[\mathbf{a}_M, \mathbf{a}_M, \cdots, \mathbf{a}_M]^T \in \mathbb{C}^{N\times 1}$ is a (elements location exchanged) repetition version of $\mathbf{a}_M$ by a factor of Q. From equation (16), we can find that $\mathbf{H}_U$ is transformed to a diagonal matrix $\tilde{\mathbf{H}}_U$ with the matrix exchange operation. Thus, by considering *any* consecutive M rows from $\mathbf{y}_U$, the transmitted signals can be detected by using one-tap channel equalization without generating interference. However, according to (14), the elements power of $\tilde{\mathbf{\Upsilon}}$ could be different and the frequency selectivity among subcarriers will be generated. In order to maximize the signal power, it is better to select the edge M rows. On the other hand, it shows that the power of $\mathbf{a}_M$ is expanded across the whole bandwidth (i.e., by vector $\tilde{\mathbf{a}}_M$). It implies that interference will be generated by such a system to the whole bandwidth, and thus a subband filter could be adopted to reduce the OoBE and interference to other users.

Next, we consider the generalized circular convolution property with the down-sampling operation (G-CCP-DS). We define $\mathbf{B}$, $\mathbf{F}_N$, $\mathbf{J}^{(u)}$, $\mathbf{\Phi}_\eta$, $\mathbf{F}_M$ and $\mathbf{H}_O$ have the same meaning as in Theorem 1. In addition, define $\mathbf{D}_Q \in \mathbb{R}^{M\times N}$ as the down-sampling matrix by a factor of Q, which can be formed as:

$$\mathbf{D}_Q = \begin{pmatrix} \mathbf{1}_d & 0 & \cdots & 0 \\ 0 & \mathbf{1}_d & \cdots & 0 \\ \vdots & \vdots & \ddots & \vdots \\ 0 & 0 & \cdots & \mathbf{1}_d \end{pmatrix}, \tag{18}$$

and $\mathbf{1}_d = [1, 0, 0, \cdots, 0]_{1\times Q}$. Similarly, the size of $\mathbf{D}_Q$ could vary in different cases. We can have the following Theorem:

Theorem 2 (G-CCP-DS) *Define $\mathbf{H}_D = \mathbf{F}_M^H \mathbf{D}_Q \mathbf{\Phi}_\eta \mathbf{B}\mathbf{F}_N$, then we have the following generalized downsampling circular convolution property*

$$\mathbf{H}_D = \mathbf{F}_M^H \mathbf{D}_Q \mathbf{\Phi}_\eta \mathbf{B}\mathbf{F}_N = \frac{1}{\sqrt{Q}} \mathbf{\Gamma}\mathbf{H}_O \ , \tag{19}$$

where $\mathbf{\Gamma} = [\mathbf{I}_M, \mathbf{I}_M, \cdots, \mathbf{I}_M]\mathbf{J}^{(u)}$ is a repetition version of identity matrix $\mathbf{I}_M$ by a factor of Q (elements location exchanged).

Proof: See Appendix B. ∎

Theorem 2 implies that G-CCP-DS is very similar to G-CCP-US except that its elements are not weighted. Similarly, to apply the Theorem 2 in telecommunication systems, we assume that in a complete multicarrier communication system where the transmitter sampling rate is Q times as that of the receiver's, and $\mathbf{a}_N \in \mathbf{C}^{N\times 1}$ is the transmit signal vector, $\mathbf{B}$ is

the channel matrix and $\mathbf{\Phi}_\eta$ is applied to shift the signal to the allocated subcarriers. Thus, the received signal can be written as:

$$\mathbf{y}_D = \mathbf{F}_M^H \mathbf{D}_Q \mathbf{\Phi}_\eta \mathbf{B} \mathbf{F}_N \mathbf{a}_N = \frac{1}{\sqrt{Q}} \mathbf{\Gamma} \mathbf{H}_O \mathbf{a}_N \ , \tag{20}$$

By using simple matrix exchange operation, (20) can be equivalently expressed as the following multiplication

$$\mathbf{y}_D = \frac{1}{\sqrt{Q}} \sum_{l=0}^{Q-1} \mathbf{H}_D(l) \tilde{\mathbf{a}}_N(l) \ , \tag{21}$$

where $\mathbf{H}_D(l) \in \mathbb{C}^{M \times M}$ is a **diagonal** matrix by taking the $(lM+1)$-th to $(l+1)M$-th diagonal elements of $\mathbf{H}_D = \text{diag}(\mathbf{J}^{(u)}\mathbf{h}_F)$ as its diagonal elements. $\tilde{\mathbf{a}}_N(l)$ is the l-th sub-vector of $\tilde{\mathbf{a}}_N = \mathbf{J}^{(u)}\mathbf{a}_N$ by taking its $(lM+1)$-th to $(l+1)M$-th elements. From equation (21), we can find that even with the DFT/IDFT pair mismatch at the left and right of the circular matrix $\mathbf{B}$, the circular convolution property still holds in a generic sense. However, due to the receiver bandwidth reduction, the transmitter signals are aliased at the receiver. To avoid signal aliasing, *any* consecutive M non-zero element in $\mathbf{a}_N$ can be sent. In such cases, the received signal will be degraded as $\mathbf{y}_D = \mathbf{H}_O(l)\mathbf{a}_N(l)$ and one-tap interference free channel equalizer can be applied. Again, when $Q = 1$ and $\eta = 0$, equation (19) will be reduced to the O-CCP.

G-CCP-US and G-CCP-DS in Theorem 1 and 2, respectively, build a foundation for the physical layer RAN slicing system with the transmitter and receiver sampling rate (and system bandwidth) mismatch. In the sequel, based on Theorem 1 and 2, we will derive the system model, equalizer, and interference cancellation algorithms for the most generic scenario (i.e., DBDR), by considering both BB and RF configuration differences between slices. In addition, we will also present detailed performance analyses with novel insights.

IV. Uplink RAN Slicing System

A. DBDR System Model

Assume the transmitting signals vector for slice 1 and 2 are $\mathbf{a}_1 \in \mathbb{C}^{M_1 \times 1}$ and $\mathbf{a}_2 \in \mathbb{C}^{M_2 \times 1}$, respectively. Following the traditional CP-OFDM procedure of IDFT and CP insertion, as shown in Fig. 3, the signals at two UEs can be written in matrix form as:

$$\bar{\mathbf{b}}_1 = \mathbf{C}_1 \mathbf{\Psi}_1 \tilde{\mathbf{F}}_{N_{U1}} \mathbf{a}_1 \ ; \quad \bar{\mathbf{b}}_2 = \bar{\mathbf{C}}_2 \mathbf{F}_{N_{U2}} \mathbf{a}_2 \ , \tag{22}$$

where $\tilde{\mathbf{F}}_{N_{U1}} \in \mathbb{C}^{N_{U1} \times M_1}$ is the first M_1 columns of the N_{U1}-point normalized IDFT matrix. The function of $\mathbf{\Psi}_1$ is to shift the signals to the corresponding frequency spectrum to where the slice is assigned. Note that the frequency shift at UE 2 is actually performed by the RF component, which will be explained later.

The CP insertion matrices for the two UEs are $\mathbf{C}_1 = [\mathbf{0}_{L_{CP,1} \times (N_{U1} - L_{CP,1})}, \mathbf{I}_{L_{CP,1}}; \mathbf{I}_{N_{U1}}]$, and $\bar{\mathbf{C}}_2 = [\mathbf{0}_{L_{CP,2} \times (N_{U2} - L_{CP,2})}, \mathbf{I}_{L_{CP,2}}; \mathbf{I}_{N_{U2}}]$, respectively. Note that the semicolons in CP expressions denote the transpose operation. $L_{CP,1}$ and $L_{CP,2}$ are the CP length in *UE samples*. One should note that the sample duration of UE 2 is Q times longer than that of UE 1 (as shown in Fig. 2).

As shown in Fig. 3, with a low OoBE subband filtering (i.e., F-OFDM), we can write the output of the subband filter for the two slices as

$$\bar{\mathbf{c}}_1 = \mathbf{A}_1 \bar{\mathbf{b}}_\mathbf{1} + \boldsymbol{\xi}_1 \quad \text{and} \quad \bar{\mathbf{c}}_2 = \mathbf{A}_2 \tilde{\mathbf{\Psi}}_2 \mathbf{U}_Q \bar{\mathbf{b}}_\mathbf{2} + \boldsymbol{\xi}_2 \ , \tag{23}$$

where $\mathbf{A}_i \in \mathbb{C}^{L_i \times L_i}$ is a matrix form of subband filtering operation. It is a Toeplitz matrix with its first column and first row being $[\mathbf{g}_{Ti}; \mathbf{0}_{(L_i - N_{Bi}) \times 1}]$ and $[g_{Ti}(1), \mathbf{0}_{1 \times (L_i - 1)}]$, respectively. $\tilde{\mathbf{\Psi}}_2 \in \mathbb{C}^{L_2 \times L_2}$ is the equivalent frequency shifter at UE 2, and its i-th diagonal element is $e^{j \cdot 2\pi (i - Q L_{CP,2} - 1)\eta_2 / N_{B2}}$. $\boldsymbol{\xi}_1$ and $\boldsymbol{\xi}_2$ are the inter-symbol-interference (ISI) generated from the filter tails in the F-OFDM system. With proper filter and system frame structure design, ISI is negligible and thus will be omitted in this paper to focus on the ISBI, i.e., $\boldsymbol{\xi}_1 = \boldsymbol{\xi}_2 = \mathbf{0}$. However, the detailed analysis of ISI for UFMC based DBSR system can be found in [8]. As shown in Fig. 3, $\mathbf{A}_2 \tilde{\mathbf{\Psi}}_2 \mathbf{U}_Q \bar{\mathbf{b}}_\mathbf{2}$ denotes equivalent digital domain implementation, where the digital subband filter $\mathbf{A}_2$ replaces RF filter with equivalent filter response in the digital domain.

According to equation (5), the symbol duration of the slice 2 is G times as long as that of slice 1. To completely express the system model and analyze the interference, it is necessary to consider at least G symbols in the first slice (e.g., in Fig. 2, $G = 2$.). Let us denote $\bar{\mathbf{c}}_{g1}$ as a vector formed by contiguous G symbols in slice 1, i.e. $\bar{\mathbf{c}}_{g1} = [\bar{\mathbf{c}}_1(0), \bar{\mathbf{c}}_1(1), \cdots, \bar{\mathbf{c}}_1(G-1)]^T$.

Let us define multi-path fading channel impulse responses of the two UEs to the BS as $\mathbf{h}_{T1}$ and $\mathbf{h}_{T2}$, respectively, and the channel gain $\mathbb{E}[\mathbf{h}_{T1}^H \mathbf{h}_{T1}] = \rho_1^2$ and $\mathbb{E}[\mathbf{h}_{T2}^H \mathbf{h}_{T2}] = \rho_2^2$. In addition, $\bar{\mathbf{B}}_i$ is the equivalent Toeplitz channel matrix. Then the received signal at the base station can be written as

$$\bar{\mathbf{x}} = \mathbf{h}_{T1} * \bar{\mathbf{c}}_{g1} + \mathbf{h}_{T2} * \bar{\mathbf{c}}_2 + \bar{\mathbf{w}} = \bar{\mathbf{B}}_1 \bar{\mathbf{c}}_{g1} + \bar{\mathbf{B}}_2 \bar{\mathbf{c}}_2 + \bar{\mathbf{w}} \ , \tag{24}$$

where $\bar{\mathbf{w}}$ is the noise vector with its element having a distribution $\bar{w}(i) \sim \mathcal{CN}(0, \sigma^2)$.

At the BS receiver, due to different baseband configurations and symbol duration, the processing of the received two slice signals also varies. Specifically, $\bar{\mathbf{x}}$ contains G symbols for slice 1 and only 1 symbol for slice 2. To detect the signal on the first slice, the received signal will be split into G non-overlapping L_1 length symbols (as shown in Fig. 2), and each of them can be processed following the normal receiver procedure of filtered OFDM. Let us define $\bar{\mathbf{x}}_k$ as the $(kL_1 + 1)$-th to $(k+1)L_1$-th element of $\bar{\mathbf{x}}$. Then the signal (before channel equalization) of the k-th symbol of the first UE can be written as

$$\bar{\mathbf{y}}_{1,k} = \tilde{\mathbf{F}}_{N_{B1}}^H \mathbf{\Psi}_1^H \mathbf{R}_1 \mathbf{A}_1^H \bar{\mathbf{x}}_k \ , \text{for} \quad k = 0, \cdots, G-1 \ , \tag{25}$$

where $\mathbf{R}_1$ and $\mathbf{A}_1^H$ are the CP removal and matched filter matrices[8] with correct dimension, respectively.

For the second slice assigned to the second UE, the length of $\bar{\mathbf{x}}$ is the same as UE 2's symbol. After the subband filtering, CP removal, and DFT, the signal of the second slice before channel equalization can be written as

$$\bar{\mathbf{y}}_2 = \tilde{\mathbf{F}}_{N_{B2}}^H \mathbf{\Psi}_2^H \bar{\mathbf{R}}_2 \mathbf{A}_2^H \bar{\mathbf{x}} \ , \tag{26}$$

[8]One should note that arbitrary subband filters can be adopted at the receiver beside the matched filter. Especially to align the 3GPP standardization that waveform should be transparent [17]. However, without loss generality, we use matched filters here to make our expression compact and the extension is straightforward.

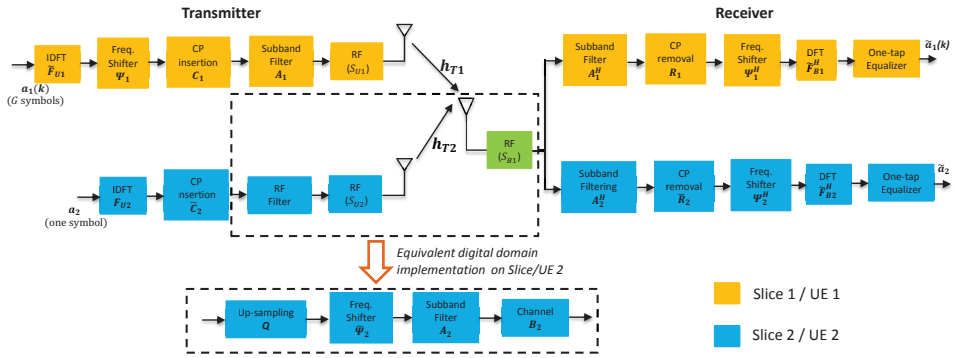

Fig. 3. Transmitter and receiver block diagram of DBDR physical layer network slicing for uplink transmission. (Note that the downlink transmission case is similar, thus, is omitted in this paper for brevity.)

where $\bar{\mathbf{R}}_2 = [\mathbf{0}_{N_{B2}\times QL_{CP,2}}, \mathbf{I}_{N_{B2}}]$ is the matrix for CP removal. Note that the CP length (in samples) at the BS is Q times the size as that of the UE due to the sampling rate mismatch. $\tilde{\mathbf{F}}^H_{N_{B2}} \in \mathbb{C}^{M_2\times N_{B2}}$ is a sub-matrix of normalized N_{B2}-point DFT matrix $\mathbf{F}^H_{N_{B2}}$ by taking its first M_2 rows.

B. One-tap Channel Equalization

By using the generalized circular convolution property in Theorem 1, we prove in Appendix C that the frequency domain system model for slice 1 and 2 signals can be expressed as

$$\bar{\mathbf{y}}_{1,k} = \mathbf{H}_{eff,1}\mathbf{a}_1(k) + \bar{\mathbf{v}}_{1,k} + \bar{\mathbf{w}}_{1,k}\ ,\quad k = 0, \cdots, G-1 \quad (27)$$

and

$$\bar{\mathbf{y}}_2 = \mathbf{H}_{eff,2}\boldsymbol{\Upsilon}_0\mathbf{a}_2 + \bar{\mathbf{v}}_2 + \bar{\mathbf{w}}_2\ , \quad (28)$$

where the *diagonal* phase shifting matrix $\boldsymbol{\Upsilon}_0 = \text{diag}(\boldsymbol{\upsilon}_0)$. The *diagonal* matrices

$$\mathbf{H}_{eff,1} = \frac{1}{\sqrt{Q}}\mathbf{H}_1\mathbf{G}_1^H\mathbf{G}_1 \ \text{ and } \ \mathbf{H}_{eff,2} = \frac{1}{\sqrt{Q}}\mathbf{H}_2\mathbf{G}_2^H\mathbf{G}_2 \quad (29)$$

are the effective channels by taking the subband filters into account. $\mathbf{H}_1 = \sqrt{N_{B1}}\text{diag}[\tilde{\mathbf{F}}^H_{N_{B1}}\boldsymbol{\Psi}_1^H\mathbf{h}_1]$ and $\mathbf{H}_2 = \sqrt{N_{B2}}\text{diag}[\tilde{\mathbf{F}}^H_{N_{B2}}\boldsymbol{\Psi}_2^H\mathbf{h}_2]$ are the frequency channel responses at the respective subcarriers. $\mathbf{G}_1 = \sqrt{N_{B1}}\text{diag}[\tilde{\mathbf{F}}^H_{N_{B1}}\mathbf{g}_{T1,p}]$ and $\mathbf{G}_2 = \sqrt{N_{B2}}\text{diag}[\tilde{\mathbf{F}}^H_{N_{B2}}\mathbf{g}_{T2,p}]$ are the frequency filter responses at the respective subcarriers.

$\bar{\mathbf{v}}_{1,k} = \tilde{\mathbf{F}}^H_{N_{B1}}\boldsymbol{\Psi}_1^H\mathbf{R}_1\mathbf{A}_1^H\bar{\mathbf{B}}_{2,k}\bar{\mathbf{c}}_2$ is the ISBI on the k-th symbol of slice 1 from slice 2, where $\bar{\mathbf{B}}_{2,k}$ is a sub-matrix of $\bar{\mathbf{B}}_2$ obtained by taking its (kL_1+1)-th to $(k+1)L_1$-th rows. On the other hand, $\bar{\mathbf{v}}_2 = \tilde{\mathbf{F}}^H_{N_{B2}}\boldsymbol{\Psi}_2^H\bar{\mathbf{R}}_2\mathbf{A}_2^H\bar{\mathbf{B}}_1\bar{\mathbf{c}}_{g1}$ is the ISBI from slice 1 to slice 2. $\bar{\mathbf{w}}_{1,k} = \tilde{\mathbf{F}}^H_{N_{B1}}\boldsymbol{\Psi}_1^H\mathbf{R}_1\mathbf{A}_1^H\bar{\mathbf{w}}_k$ and $\bar{\mathbf{w}}_2 = \tilde{\mathbf{F}}^H_{N_{B2}}\boldsymbol{\Psi}_2^H\bar{\mathbf{R}}_2\mathbf{A}_2^H\bar{\mathbf{w}}$ are the noise after DFT and receiver filtering process at slices 1 and 2, respectively.

C. Frequency Selectivity Analysis and Proposed Power Compensation Algorithm

By using $\mathbb{E}\{\mathbf{H}_1\mathbf{H}_1^H\} = \rho_1^2\mathbf{I}_{M1}$ and $\mathbb{E}\{\mathbf{H}_2\mathbf{H}_2^H\} = \rho_2^2\mathbf{I}_{M2}$, it is easy to obtain the desired signal power gain at each subcarrier as

$$\bar{\boldsymbol{\alpha}}_1 = \mathbb{E}\{\text{diag}|\mathbf{H}_{eff,1}|^2\} = \frac{\rho_1^2}{Q}\text{diag}|\mathbf{G}_1^H\mathbf{G}_1|^2 \quad (30)$$

and

$$\bar{\boldsymbol{\alpha}}_2 = \mathbb{E}\{\text{diag}|\mathbf{H}_{eff,2}\boldsymbol{\Upsilon}_0|^2\} = \frac{\rho_2^2}{Q}\text{diag}|\mathbf{G}_2^H\mathbf{G}_2\boldsymbol{\Upsilon}_0|^2\ . \quad (31)$$

Thanks to the generalized circular convolution property in Theorem 1, equations (27) and (28) reveal that one-tap channel equalization is still applicable in the DBDR scenario without generating extra ICI. However, unlike the OFDM system, the subband filtering operation at F-OFDM system and sampling rate mismatch may introduce the frequency selectivity among the subcarriers in both slices. Taking slice 2 as an example, the filter gain $|\mathbf{G}_2^H\mathbf{G}_2\boldsymbol{\Upsilon}_0|^2$ at each subcarrier may be different, and typically, the power at the edge subcarriers is smaller than the ones in the middle as a side effect of ISBI rejection, as shown in Fig. 4a. In addition, a phase shift $\boldsymbol{\Upsilon}_0$ at slice 2 may further introduce the power distribution imbalance among the subcarriers. According to equation (14), the power at each subcarrier is shown in Fig. 4b with different Q. Larger mismatch factor Q leads to slightly larger frequency selectivity. The combined effect of both filter and phase shift is shown in red in Fig. 4b.

The noise power at the two slices can be expressed as

$$\bar{\boldsymbol{\beta}}_1 = \mathbb{E}\{\text{diag}(\bar{\mathbf{w}}_{1,k}\bar{\mathbf{w}}_{1,k}^H)\} = \frac{\sigma^2}{Q}\text{diag}|\mathbf{G}_1^H\mathbf{G}_1| \quad (32)$$

and

$$\bar{\boldsymbol{\beta}}_2 = \mathbb{E}\{\text{diag}(\bar{\mathbf{w}}_2\bar{\mathbf{w}}_2^H)\} = \frac{\sigma^2}{Q}\text{diag}|\mathbf{G}_2^H\mathbf{G}_2|\ . \quad (33)$$

According to (30), (31), (32) and (33), receiver filtering will cause both desired signal and noise selectivity, which will mitigate the overall selectivity in terms of the SNR (signal to noise ratio) that can be partly compensated.

With the symbol duration difference in the DBDR scenario, it is complex to analyze the ISBI. Due to the space limit, the DBDR ISBI analysis will be omitted here. However, we will analyze the ISBI in the SBDR case in the next subsection. Another consideration is that with guardband, the ISBI level can be significantly reduced, as shown later in Section VI. Nevertheless, the ISBI expressions for DBSR is derived in detail in [8].

The selectivity among the subcarriers could be very significant and leads to inefficient power allocation since some subcarriers will receive more gain than the others, as shown in Fig. 4. To further improve the performance via equal output $\mathbf{S}\bar{\mathbf{N}}\mathbf{R}_i$ at the receiver, we propose the power pre-compensation algorithms at the transmitter side to pre-cancel the gain differences. Specifically, the unified precoding matrices can be

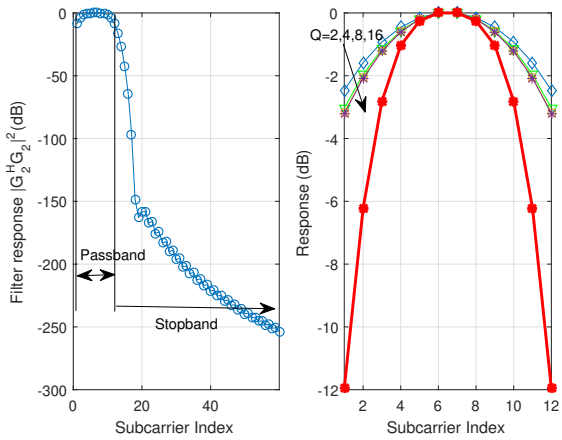

Fig. 4. Filter and phase shift frequency responses versus subcarrier index ($M_2 = 12$): a) Filter frequency response diag$|\mathbf{G}_2^H\mathbf{G}_2|^2$ (F-OFDM system [23]); b), Phase shift diag$|\boldsymbol{\Upsilon}_0|^2$ response with $Q = 2, 4, 8, 16$, and joint response diag$|\mathbf{G}_2^H\mathbf{G}_2\boldsymbol{\Upsilon}_0|^2$ (in red, where we consider $Q = 16$.).

expressed as

$$\bar{\mathbf{E}}_1 = \vartheta\left[\sqrt{\frac{M_1}{\text{trace}[(\mathbf{G}_1\mathbf{G}_1^H)^{-1}]}}|\mathbf{G}_1|^{-1} - \mathbf{I}_{M_1}\right] + \mathbf{I}_{M_1}$$

$$\bar{\mathbf{E}}_2 = \vartheta\left[\sqrt{\frac{M_2}{\text{trace}[(\mathbf{G}_2\mathbf{G}_2^H\boldsymbol{\Upsilon}_0\boldsymbol{\Upsilon}_0^H)^{-1}]}}|\mathbf{G}_2\boldsymbol{\Upsilon}_0|^{-1} - \mathbf{I}_{M_2}\right] + \mathbf{I}_{M_2}, \quad (34)$$

where $\vartheta = 1$ and $\vartheta = 0$ refer to with and without power compensation, respectively. Hence, $\bar{\mathbf{E}}_1\mathbf{a}_1$ and $\bar{\mathbf{E}}_2\mathbf{a}_2$ will be transmitted instead of $\mathbf{a}_1$ and $\mathbf{a}_2$.

D. ISBI Analysis and Cancellation for SBDR Scenario

In this subsection, we will degrade the DBDR system to the SBDR system by taking $G = 1$. An example of the SBDR system is the NB-IoT, where the same subcarrier spacing and symbol duration are used for both LTE and IoT slices. However, IoT may use significantly smaller RF bandwidth than the normal LTE system to save cost/complexity/energy consumption. Next, we will derive the ergodic ISBI expressions, and a collaboration based ISBI cancellation algorithm will be proposed at the BS side to guide the system design.

By taking $G = 1$, the symbol duration and DFT size of the two slices are the same, i.e., $\Delta T_1 = \Delta T_2$ and $N_{B1} = N_{B2}$. Besides, $\bar{\mathbf{c}}_{g1} = \bar{\mathbf{c}}_1(k) = \bar{\mathbf{c}}_1$, $\bar{\mathbf{v}}_{1,k} = \bar{\mathbf{v}}_1$, $\bar{\mathbf{w}}_{1,k} = \bar{\mathbf{w}}_1$ for $k = 0, 1, \cdots, G-1$. By using the generalized circular convolution property of Theorem 1, the ISBI terms can be rewritten as

$$\bar{\mathbf{v}}_1 = \frac{1}{\sqrt{Q}}\tilde{\mathbf{H}}_2\mathbf{G}_1^H\mathbf{G}_{S,2}\boldsymbol{\Upsilon}_I\bar{\mathbf{E}}_2\mathbf{a}_2 \,, \quad (35)$$

$$\bar{\mathbf{v}}_2 = \mathbf{0} \,, \quad (36)$$

where $\tilde{\mathbf{H}}_2 = \sqrt{N_{B1}}\text{diag}[\tilde{\mathbf{F}}_{N_{B1}}^H\boldsymbol{\Psi}_1^H\mathbf{h}_2]$ is the frequency channel response of $\mathbf{h}_2$ at the first slice's passband. $\mathbf{G}_{S,2} = \sqrt{N_{B1}}\text{diag}[\tilde{\mathbf{F}}_{N_{B1}}^H\boldsymbol{\Psi}_1^H\mathbf{g}_{T2}]$ is the frequency domain response of the *second* slice's filter $\mathbf{g}_{T2}$ at the *first* slice's frequency band. $\boldsymbol{\Upsilon}_I \in \mathbb{C}^{M_1\times M_2}$ is the exchange matrix by taking the (η_1+1)-th to the (η_1+M_1)-th columns and rows of $\mathbf{J}^{(u)}\boldsymbol{\Upsilon}$.

Equations (35) and (36) show that slice 2 is free of the interference from slice 1. The reason is simple, the signal at slice 1 is transmitted and processed with matched sampling rate at the BS, which enforces the orthogonality among slices. However, slice 2 with mismatched sampling rate at transmitter and receiver will generate the ISBI to slice 1. By noting the fact that each row in $\boldsymbol{\Upsilon}_I$ has only one non-zero element, the interference is also expressed as a multiplication between the channel, filter response and signal $\mathbf{a}_2$. According to Fig. 4 a, the interference level will be significantly reduced since $\mathbf{G}_{S,2}$ is located in the filter stopband.

The interference power at the subcarriers of slice 2 can be derived as

$$\boldsymbol{\gamma}_1 = \text{diag}\{\mathbb{E}[\bar{\mathbf{v}}_1\bar{\mathbf{v}}_1^H]\} = \frac{\rho_2^2}{Q}|\mathbf{G}_1^H\mathbf{G}_{S,2}|^2\tilde{\boldsymbol{\Upsilon}}_I \,. \quad (37)$$

One should note that $\tilde{\boldsymbol{\Upsilon}}_I = \boldsymbol{\Upsilon}_I\bar{\mathbf{E}}_2\bar{\mathbf{E}}_2^H\boldsymbol{\Upsilon}_I^H$ is an M_1-dimensional diagonal matrix. The interference level depends on the guardband between the two slices. Larger ΔB_1 can mitigate the ISBI power $\boldsymbol{\gamma}_1$ since it will push $\mathbf{G}_{S,2}$ far away from the filter passband, as shown in Fig. 4a. By using equations (30), (31), (32), (33) and (37), we can write the channel ergodic output signal to interference plus noise ratio (SINR) at the two slices as

$$\mathbf{S\bar{I}\bar{N}R}_1 = \frac{\rho_1^2|\mathbf{G}_1\mathbf{G}_1^H\bar{\mathbf{E}}_1|^2}{\rho_2^2|\mathbf{G}_1^H\mathbf{G}_{S,2}|^2\tilde{\boldsymbol{\Upsilon}}_I + \sigma^2|\mathbf{G}_1\mathbf{G}_1^H|}$$

$$\mathbf{S\bar{I}\bar{N}R}_2 = \mathbf{S\bar{N}R}_2 = \frac{\rho_2^2}{\sigma^2}|\mathbf{G}_2^H\mathbf{G}_2\bar{\mathbf{E}}_2|^2 \,. \quad (38)$$

With limited guardband between slice 1 and 2, the interference $\boldsymbol{\gamma}_1$, especially at the edge of the slice's band, could be significant. With the given framework on the system model in (27), (28), (35), and (36), we can easily propose a low complexity but effective ISBI cancellation algorithm at the BS. Specifically, we can detect the interference free symbols at slice 2 as the first step, for the interfered signal in slice 1, we can subtract the interference $\bar{\mathbf{v}}_1$ (35) from the received signal $\bar{\mathbf{y}}_1$ in (27), i.e.,

$$\bar{\bar{\mathbf{y}}}_1 = \bar{\mathbf{y}}_1 - \bar{\mathbf{v}}_1 \,. \quad (39)$$

It is worth to mention that each subcarrier (e.g., each element in $\bar{\bar{\mathbf{y}}}_1$) is only affected by one subcarrier in slice 2 (e.g., one element of $\mathbf{a}_2$), since only one element in each row of $\boldsymbol{\Upsilon}_I$ is non-zero. Due to the page limit, the detailed per subcarrier calculation is omitted here. However, based on this property, one can propose more complex and advanced ISBI cancellation algorithms. Besides, although there are other interference cancellation methods for the mixed-numerology system, they are either based on overlapping multiplexing model (e.g., [15]) or with different assumptions of numerology configurations with this paper (e.g., [24]). Hence, the performance of the interference cancellation method in this paper is not comparable with the ones in other researches.

V. Downlink RAN Slicing System

A. DBDR System Model, Equalization, and Power Compensation Algorithm

Due to the non-reciprocity of the uplink and downlink transmission in the physical layer RAN slicing system, it is necessary to separately derive the downlink system model, equalizer, interference analysis and interference cancellation algorithm.

At the transmitter side (i.e., BS), the signal in the i-th service/slice after IDFT, CP insertion and subband filtering can be written in matrix form as:

$$\hat{\mathbf{c}}_1 = \mathbf{A}_1^H \mathbf{C}_1 \mathbf{\Psi}_1 \tilde{\mathbf{F}}_{N_{B1}} \mathbf{a}_1 \; ; \quad \hat{\mathbf{c}}_2 = \mathbf{A}_2^H \hat{\mathbf{C}}_2 \mathbf{\Psi}_2 \tilde{\mathbf{F}}_{N_{B2}} \mathbf{a}_2 \; , \quad (40)$$

where $\hat{\mathbf{C}}_2 = [\mathbf{0}_{QL_{CP,2}\times(N_{B2}-QL_{CP,2})}, \mathbf{I}_{QL_{CP,2}}; \mathbf{I}_{N_{B2}}] \in \mathbb{R}^{L_2 \times N_{B2}}$ is the CP insertion matrix.

Similar to the uplink transmission, we have to consider G consecutive symbols as $\hat{\mathbf{c}}_{g1} = [\hat{\mathbf{c}}_1(0), \hat{\mathbf{c}}_1(1), \cdots, \hat{\mathbf{c}}_1(G-1)]^T$. The signal in one LCM symbol [8] before transmission over the channel can be written as

$$\hat{\mathbf{x}} = \hat{\mathbf{c}}_{g1} + \hat{\mathbf{c}}_2 \; . \quad (41)$$

At the receiver, two UEs will follow different receiver processing due to different baseband and RF configurations. Specifically, at UE 1, the received signal $\mathbf{y}_1$ is split into G non-overlapping symbols, and each segment has L_1 samples. Let us define $\hat{\mathbf{x}}_k$ as the (kL_1+1)-th to $(k+1)L_1$-th element of $\hat{\mathbf{x}}$. Then the signal (before channel equalization) of the k-th symbol for $k = 0, 1, \cdots, G-1$ of the first UE can be written as

$$\hat{\mathbf{y}}_{1,k} = \tilde{\mathbf{F}}_{N_{U1}}^H \mathbf{\Psi}_1^H \mathbf{R}_1 \mathbf{A}_1 (\hat{\mathbf{B}}_1 \hat{\mathbf{x}}_k + \hat{\mathbf{w}}_{1,k}) \; , \quad (42)$$

where $\mathbf{R}_1$, $\mathbf{A}_1$ and $\hat{\mathbf{B}}_1$ are the CP removal, matched filter and channel matrices, respectively, $\hat{\mathbf{w}}_{1,k}$ is the noise vector with its element being zero-mean and σ^2 variance Gaussian variables.

The second UE assigned within the second slice has a lower RF sampling rate; the signal will be down-sampled by a factor of Q, phase shifted, and follows a filtered OFDM processing [16]. The signal of the second UE (before channel equalization) can be written as:

$$\hat{\mathbf{y}}_2 = \mathbf{F}_{N_{U2}}^H \mathbf{\Psi}_2^H \hat{\mathbf{R}}_2 \mathbf{D}_Q \mathbf{A}_2 (\hat{\mathbf{B}}_2 \hat{\mathbf{x}} + \hat{\mathbf{w}}_2) \; , \quad (43)$$

where $\mathbf{D}_Q$ is the down-sampling matrix by a factor of Q, as defined in Theorem 2. $\hat{\mathbf{R}}_2$ is the CP removal matrix with the correct dimension. $\hat{\mathbf{w}}_2$ is the noise vector with its element being zero-mean and σ^2/Q variance Gaussian variables[9].

Using the circular convolution property in Theorem 2 and following derivations in the uplink transmission, we can write (42) as:

$$\hat{\mathbf{y}}_{1,k} = \mathbf{H}_{eff,1} \mathbf{a}_1(k) + \hat{\mathbf{v}}_{1,k} + \tilde{\mathbf{w}}_{1,k} \; , \quad (44)$$

where $\mathbf{a}_1(k)$ is the k-th symbol of $\mathbf{a}_1$ in slice 1. $\hat{\mathbf{v}}_{1,k} = \tilde{\mathbf{F}}_{N_{U1}}^H \mathbf{\Psi}_1^H \mathbf{R}_1 \mathbf{A}_1 \hat{\mathbf{B}}_{2,k} \hat{\mathbf{c}}_2$ and $\tilde{\mathbf{w}}_{1,k} = \tilde{\mathbf{F}}_{N_{U1}}^H \mathbf{\Psi}_1^H \mathbf{R}_1 \mathbf{A}_1 \hat{\mathbf{B}}_1 \hat{\mathbf{w}}_{1,k}$ are the interference from the second slice and noise after DFT operation, respectively. $\hat{\mathbf{B}}_{2,k}$ is a sub-matrix of $\hat{\mathbf{B}}_2$ obtained by taking its (kL_1+1)-th to $(k+1)L_1$-th rows. The noise power has the same expression as the uplink i.e., $\hat{\boldsymbol{\beta}}_1 = \bar{\boldsymbol{\beta}}_1$.

The first term $\mathbf{H}_{eff,1}\mathbf{a}_1(k)$ is the desired signal and it can be seen that the signal can be written as a multiplication with the filter and channel frequency response. Thus, one-tap channel equalization can be performed.

For the second UE, by using Theorem 2 in (19) and similar to the UE 1, we can rewrite equation (43) as:

$$\hat{\mathbf{y}}_2 = \mathbf{H}_{eff,2} \mathbf{a}_2 + \hat{\mathbf{v}}_2 + \tilde{\mathbf{w}}_2 \; , \quad (45)$$

[9]Note that due to the reduced processing bandwidth, the equivalent noise power is also reduced accordingly.

where $\hat{\mathbf{v}}_2 = \mathbf{F}_{N_{U2}}^H \mathbf{\Psi}_2^H \hat{\mathbf{R}}_2 \mathbf{D}_G \mathbf{A}_2 \bar{\mathbf{B}}_1 \hat{\mathbf{c}}_1$ and $\tilde{\mathbf{w}}_2 = \mathbf{F}_{N_{U2}}^H \mathbf{\Psi}_2^H \hat{\mathbf{R}}_2 \mathbf{\Psi} \mathbf{D}_G \mathbf{A}_2 \hat{\mathbf{w}}_2$ are interference from the first slice and noise after DFT operation, respectively. The noise power has the same expression as the uplink, i.e., $\hat{\boldsymbol{\beta}}_2 = \bar{\boldsymbol{\beta}}_2$.

Similar to the uplink case, the power pre-equalization at the transmitter can be proposed to improve the performance of the two slices. Specifically, $\hat{\mathbf{E}}_1 \mathbf{a}_1(k)$ and $\hat{\mathbf{E}}_2 \mathbf{a}_2$ can be transmitted at the slices 1 and 2 respectively, where

$$\hat{\mathbf{E}}_i = \vartheta \Big[\sqrt{\frac{M_i}{\text{trace}[(\mathbf{G}_i \mathbf{G}_i^H)^{-1}]}} |\mathbf{G}_i|^{-1} - \mathbf{I}_{M_i} \Big] + \mathbf{I}_{M_i} \quad (46)$$

for $i = 1$ or 2. $\vartheta = 1$ when the proposed power compensation scheme is considered, otherwise $\vartheta = 0$. Hence, $\tilde{\mathbf{E}}_i \mathbf{a}_i$ instead of $\mathbf{a}_i$ will be transmitted.

B. SBDR ISBI Analysis and Cancellation

By taking $G = 1$, we have $\hat{\mathbf{c}}_{g1} = \hat{\mathbf{c}}_1(k) = \hat{\mathbf{c}}_1$, $\hat{\mathbf{v}}_1(i) = \hat{\mathbf{v}}_1$, and $N_{B1} = N_{B2}$. Also considering the power compensation matrix $\hat{\mathbf{E}}_i$ at the transmitter, and using the generalized circular convolution property in Theorem 2, the ISBI terms can be rewritten as

$$\hat{\mathbf{v}}_1 = \mathbf{0} \; ; \;\; \hat{\mathbf{v}}_2 = \frac{1}{\sqrt{Q}} \tilde{\mathbf{\Gamma}} \tilde{\mathbf{H}}_2 \mathbf{G}_2^H \mathbf{G}_{S,1} \hat{\mathbf{E}}_1 \mathbf{a}_1 \; , \quad (47)$$

where $\mathbf{G}_{S,1} = \sqrt{N_{B2}} \text{diag}[\tilde{\mathbf{F}}_{N_{B2}}^H \mathbf{\Psi}_2^H \mathbf{g}_{T1}]$ is the frequency domain response of the *first* slice's filter at the *second* slice's band. $\tilde{\mathbf{\Gamma}}$ is a sub-matrix obtained by taking the η_2-th to $(\eta_2 + M_2)$-th columns of $\mathbf{\Gamma}$.

Unlike uplink transmission, where slice 2 is interference free, equation (47) shows that slice 1 is free of the interference from slice 2 in the downlink transmission. However, slice 2 has mismatched sampling rates at transmitter and receiver, will receive the ISBI from slice 1. The interference power at the subcarriers on slice 2 can be derived as

$$\hat{\boldsymbol{\gamma}}_2 = \frac{\rho_2^2}{Q} \text{diag} |\tilde{\mathbf{\Gamma}} \mathbf{G}_2^H \mathbf{G}_{S,1} \hat{\mathbf{E}}_1|^2 \; . \quad (48)$$

Furthermore, the SINR at two slices can be expressed in vector form as

$$\begin{aligned} \mathbf{SI\hat{N}R}_1 &= \frac{\rho_1^2}{\sigma^2} |\mathbf{G}_1^H \mathbf{G}_1 \hat{\mathbf{E}}_1|^2 \; , \\ \mathbf{SI\hat{N}R}_2 &= \frac{\rho_2^2 |\mathbf{G}_2 \mathbf{G}_2^H \hat{\mathbf{E}}_2|^2}{\rho_2^2 \text{diag}|\tilde{\mathbf{\Gamma}} \mathbf{G}_2^H \mathbf{G}_{S,1} \hat{\mathbf{E}}_1|^2 + \sigma^2 |\mathbf{G}_2 \mathbf{G}_2^H|} \; . \end{aligned} \quad (49)$$

With the established signal models in equations (44), (45) and (47), we can propose a low complexity precoding algorithm at the BS to cancel the ISBI on slice 2. Specifically, we introduce a precoding matrix $\mathbf{P}_{pre}$ to the collaboration signal model by considering both slice 1 and slice 2 signals as follows

$$\hat{\mathbf{y}}_{all} = \begin{pmatrix} \mathbf{H}_1 & \mathbf{0} \\ \mathbf{0} & \mathbf{H}_2 \end{pmatrix} \cdot \underbrace{\begin{pmatrix} \hat{\mathbf{Z}}_{11} & \mathbf{0} \\ \hat{\mathbf{Z}}_{21} & \hat{\mathbf{Z}}_{22} \end{pmatrix}}_{\hat{\mathbf{Z}}} \mathbf{P}_{pre} \begin{pmatrix} \hat{\mathbf{E}}_1 \mathbf{a}_1 \\ \hat{\mathbf{E}}_2 \mathbf{a}_2 \end{pmatrix} + \begin{pmatrix} \mathbf{w}_1 \\ \mathbf{w}_2 \end{pmatrix} \; , \quad (50)$$

where $\hat{\mathbf{Z}}_{11} = \mathbf{I}_{M_1}$, $\hat{\mathbf{Z}}_{21} = \tilde{\mathbf{\Gamma}} \mathbf{G}_2^H \mathbf{G}_{S,1}$, $\hat{\mathbf{Z}}_{22} = \mathbf{I}_{M_2}$. Note that here we use the assumption $\mathbf{H}_2 = \hat{\mathbf{H}}_2$ due to the fact that the interference is only generated within a very small adjacent bandwidth [8], thus, we can assume it is within the coherent

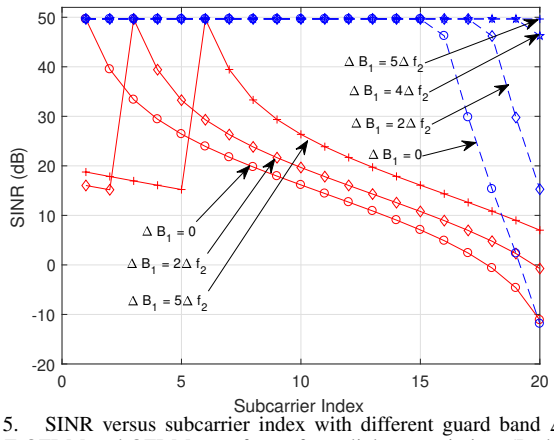

Fig. 5. SINR versus subcarrier index with different guard band ΔB_1 for both F-OFDM and OFDM waveforms for uplink transmission. (Red lines are for OFDM and blue dashed lines are for F-OFDM.)

bandwidth. Therefore, we can precancel the ISBI based on the channel independent mixture matrix $\hat{\mathbf{Z}}$ only by the following zero-forcing (ZF) criterion

$$\mathbf{P}_{pre} = (\hat{\mathbf{Z}})^{-1} . \tag{51}$$

Nevertheless, one can design a global optimal $\mathbf{P}_{pre}$ by taking both channel and mixture matrix into consideration, but at the cost of increased computation and system overhead.

VI. Numerical Results

In this section, we verify the established physical layer RAN slicing system model, the proposed power compensation algorithms and the ISBI cancellation algorithms for both uplink and downlink transmissions. Both OFDM and F-OFDM waveforms are considered for comparison purposes. F-OFDM waveform with a matched filter at the receiver is considered for all simulations with windowed Sinc filter, and the filter length equals to half of the DFT size [23]. We consider the first and the second UEs are allocated with 20% and 5% of the full bandwidth, i.e., $B_1 = 0.2$ and $B_2 = 0.05$, respectively. Each slice contains 20 subcarriers. Thus, the subcarrier spacing for the two services satisfies $\Delta f_1 = 4\Delta f_2$. In addition, we assume the RF up-/down-sampling factor in UE 2 is 20, i.e., the sampling rate at UE 2 is only 5% of the one used at the BS. The CP overhead is 10% for both slices and for both waveforms. For the special case SBDR, the two slices have the same symbol duration and subcarrier spacing, and we assume both slices occupy 5% of the full bandwidth. Considering the nature of the user cases, the modulation scheme for slices 1 and 2 are 16-QAM (quadrature amplitude modulation) and QPSK (quadrature phase shift keying), respectively. We use the LTE extended pedestrian A (EPA) channel unless otherwise specified. The minimum mean square error (MMSE) based one-tap channel equalizer is adopted for all cases. For the numerical results in this section, each point was achieved by at least 10000 simulation realizations.

We use waveform, slice number and algorithm combinations as figure legend to make it more compact, e.g., F-OFDM$_1$+ (34) means the performance at slice 1 with the proposed power pre-compensation algorithm in equation (34) based on the F-OFDM waveform.

We first investigate the interference in the SBDR system caused by RF numerology mismatches. Fig. 5 shows the output

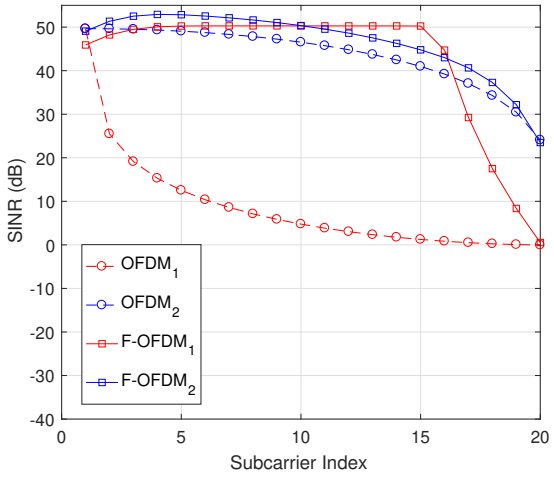

(a) F-OFDM versus OFDM without proposed algorithms

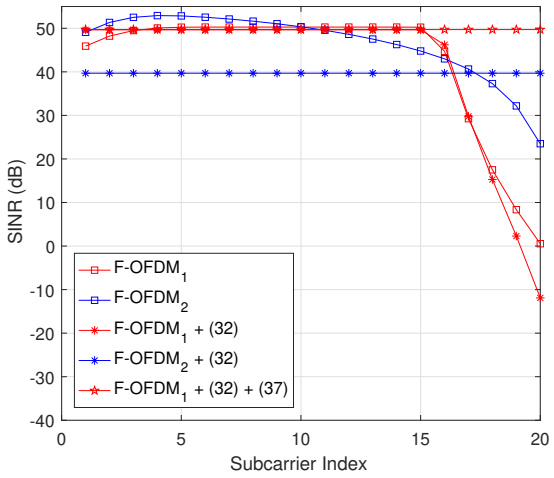

(b) F-OFDM with proposed algorithms

Fig. 6. SINR versus subcarrier index with and without proposed algorithms for both F-OFDM and OFDM waveforms in uplink transmission (Red lines are for slice 1 and blue lines are for slice 2).

signal SINR versus the subcarrier index for slice 1 in uplink transmission, with different values of guardband ΔB_1 between slices, for both F-OFDM and OFDM systems. We assume the symbol input SNR is 50 dB to make the system interference limited. The power compensation algorithm in (34) is used, but the ISBI cancellation algorithm in (39) is not considered to show the interference distribution among subcarriers. It can be seen that the two waveforms have totally different SINR distributions. Specifically, with a given guardband, F-OFDM (shown with blue dashed lines) based system shows significantly higher SINR than its counterpart (i.e., OFDM, shown with red lines). This verifies that the F-OFDM system can mitigate ISBI by the subband filtering. In addition, the interference in the OFDM based RAN slicing system shows a circular property among the subcarriers and the lowest SINR tends to be slightly improved with guardband ΔB_1 increasing. Such a property is because of the exchange matrix $\mathbf{J}^{(u)}$ as analyzed in Theorem 1. However, the interference in the F-OFDM system is much smaller and SINR reduces sharply with

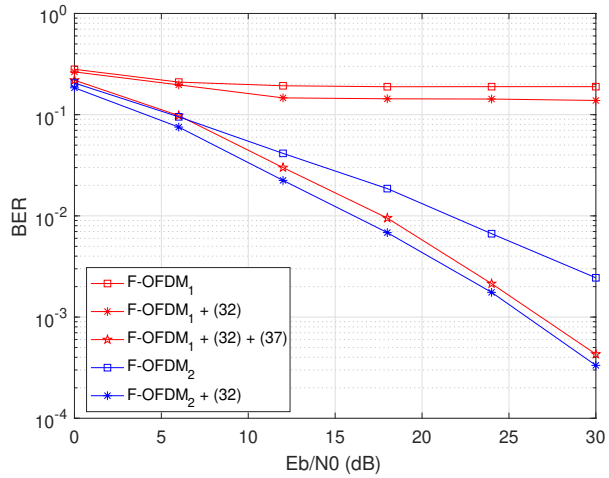

Fig. 7. BER versus E_b/N_o with and without proposed algorithms for SBDR scenario in uplink transmission (Red lines are for slice 1 and blue lines are for slice 2).

ΔB_1 increasing. It can also be observed that having 4 or 5 subcarriers as guardband between the two slices is sufficient to achieve negligible performance loss in terms of output SINR. One should also note that significant SINR reduction can be seen at the larger subcarrier index region, which is because this region is closer to the second slice's frequency band, and it receives much more interference than in the low subcarrier index [23].

By taking both power compensation and ISBI cancellation schemes into consideration, Fig. 6 depicts the output SINR against the subcarrier index. Here we use guardband $\Delta B_1 = 0$ to show the effectiveness of the proposed ISBI cancellation algorithm. For the purpose to improve the readability, we use two subfigures to depict the SINR performance, where Fig. 7(a) illustrates the SINR of F-OFDM and OFDM waveforms without any of the proposed algorithms being applied, and Fig. 7(b) shows the performance improvements of the proposed algorithms. It can be seen from Fig. 6 that the power compensation for slice 2 (and all F-OFDM based algorithm) is critical to remove the filter gain frequency selectivity. With the proposed power compensation expression (34), the SINR values among subcarriers become even. However, it is also interesting to notice that the power compensation algorithm shows negligible improvement to the slice 1 signal. This is because that for the slice 2 signal in uplink transmission, the unevenly distributed signal power results from the combination of the phase shift matrix $\boldsymbol{\Upsilon}_0$ and filter response $\mathbf{G}_2$ and $\mathbf{G}_2^H$, while only the filter responses $\mathbf{G}_1$ and $\mathbf{G}_1^H$ contribute to slice 1's signal power distribution. It can be seen from Fig. 4 that the combined effect of the phase shift matrix and filter gain is stronger than the filter gain only effect. Therefore, after compensation, the performance improvement for the former case is higher than the later. On the other hand, in the uplink the slice 1 signal suffers from interference, which further decreases the effectiveness of the power compensation algorithm. Considering the increased complexity due to the compensation algorithms, it might be a good choice to only implement the effective one in the system, i.e., $\bar{\mathbf{E}}_2$ for slice 2. The algorithm's performance in the downlink transmission can be explained following the same rationale. In addition, we can see from Fig. 6 that the proposed low complexity

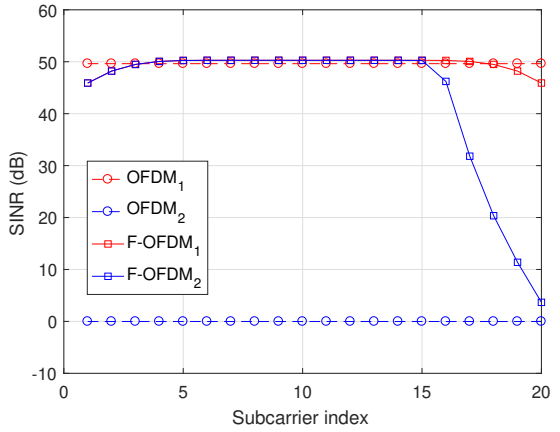

(a) F-OFDM versus OFDM without proposed algorithms

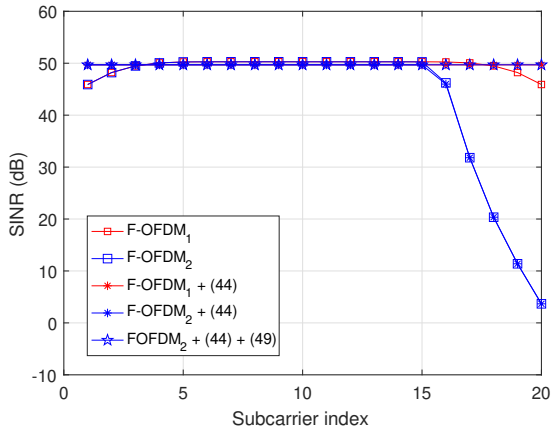

(b) F-OFDM with proposed algorithms

Fig. 8. SINR versus subcarrier index with and without proposed algorithms for both F-OFDM and OFDM waveforms in downlink transmission. (Red lines are for slice 1 and blue lines are for slice 2).)

ISBI cancellation algorithm in (39) is effective since the SINR performance is significantly improved even without any guardband protection.

The bit error rate performance in both slices for the SBDR scenario is shown in Fig. 7. The guardband between the slices is 0. Similar to the SINR performance, the curves show the effectiveness of the established system models and one-tap channel equalizer. In addition, the proposed power compensation and ISBI cancellation schemes can significantly improve the slice 2 signal's BER performance.

For the downlink case, we first investigate the SINR distribution among the subcarriers in slice 2 for both OFDM and F-OFDM based SBDR RAN slicing system in Fig. 8. Similarly, the SINR performances under different configurations are illustrated in two subfigures for better readability. One should note that slice 1 is free of interference, as shown in (47). Clearly, the OFDM based system cannot work properly due to the serious ISBI from slice 1, which verifies Theorem 2 since the signal in slice 1 will expand to the whole baseband and the interference power is equal to the desired signal power. In addition, the frequency selectivity can be compensated from (46). Nevertheless, compared with the uplink case, frequency selectivity in the downlink is less severe. Finally, the ISBI

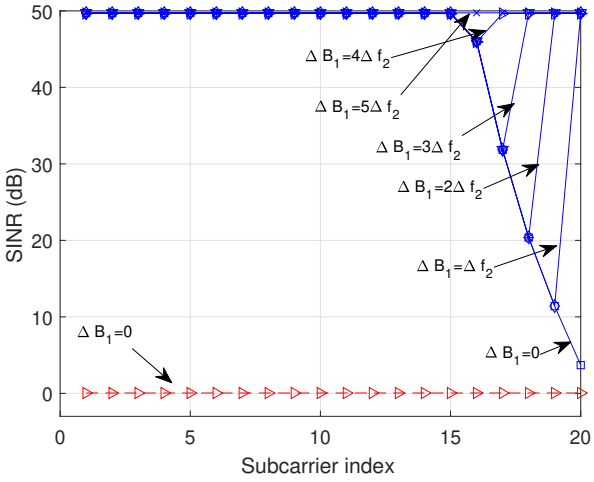

Fig. 9. SINR versus subcarrier index in downlink transmission with different guardband (Red: OFDM, Blue: Proposed).

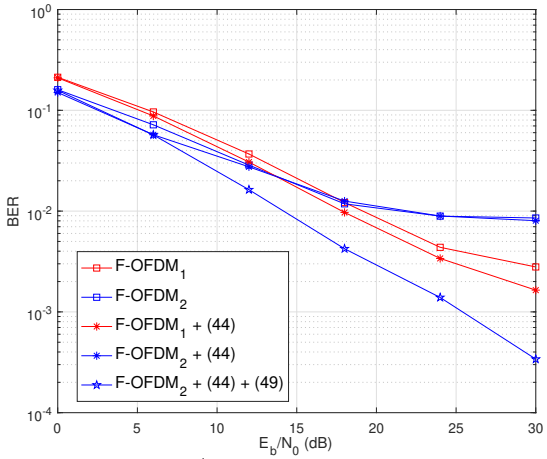

Fig. 10. BER versus E_b/N_o with and without proposed algorithms for SBDR scenario in downlink transmission (Red lines are for slice 1 and blue lines are for slice 2).

cancellation algorithm in (51) shows effectiveness since nearly the same SINR can be achieved as that in the interference free case.

The SINR at slice 2 with different guardband ΔB_1 is shown in Fig. 9 for the OFDM and F-OFDM based SBDR system. Similar to the uplink case, the minimum SINR in the F-OFDM system improves dramatically as ΔB_1 increases. Furthermore, having 4 or 5 subcarriers as guardband can achieve sufficiently high SINR.

In terms of the BER performance, Fig. 10 shows the performance for the SBDR scenario based on the F-OFDM system in the downlink transmission. The guardband between the slices is 0. It can be seen that the proposed interference cancellation algorithm can significantly improve the system performance in terms of BER.

VII. Conclusions

This paper establishes a framework for RAN slicing from the physical layer perspective. The numerology relationships among slices were defined mathematically by considering both RF and BB configuration imparities, according to which one can simply set up the parameter configurations for a desired multi-numerology system. Two theorems of generalized circular convolution properties were proposed, which build a theoretic foundation for signal isolation, collaboration and detection in such kind of systems. They also imply that the implementation of the low complexity one-tap channel equalization is feasible. Based on the derivations in the paper, it is found that the interference generated from BB and RF imparities is linearly superposed in the receiver. Simulations were performed to verify the effectiveness of the proposed system model and algorithms. It is shown that in the F-OFDM based multi-numerology systems, 4-5 subcarriers' guardband between slices can reduce the ISBI to a negligible level. Also, the proposed ISBI cancellation algorithms can significantly improve the SINR performance even without any guardband protection. The work presented in this paper provides guidance for multi-numerology system design in terms of parameter and waveform selection, as well as the frame structure and algorithms design. Moreover, it presents a solution as to how the radio access network slicing can be underpinned in the physical layer in a spectrum efficient way.

Appendix A
Proof of Theorem 1

Firstly, by using $\mathbf{F}_N\mathbf{F}_N^H = \mathbf{I}_N$, we can write

$$\begin{aligned}\mathbf{H}_U =&\mathbf{F}_N^H\mathbf{B}\mathbf{\Phi}_\eta\mathbf{U}_Q\mathbf{F}_M\\ =&(\mathbf{F}_N^H\mathbf{B}\mathbf{F}_N)\cdot(\mathbf{F}_N^H\mathbf{\Phi}_\eta\mathbf{F}_N)\cdot(\mathbf{F}_N^H\mathbf{U}_Q\mathbf{F}_M).\end{aligned}$$

Since $\mathbf{B}$ is a circular matrix with the first column being $\mathbf{b}$, by using the original circular convolution property [13], we have $(\mathbf{F}_N^H\mathbf{B}\mathbf{F}_N) = \mathbf{H}_O$. Note that $\mathbf{\Phi}_\eta$ is a spectrum shifting matrix and by using (8), we have $\mathbf{F}_N^H\mathbf{\Phi}_\eta\mathbf{F}_N = \mathbf{J}^{(u)}$.

Next, let us first divide the N-point DFT matrix $\mathbf{F}_N^H$ into Q equal size sub-matrices, each taking M consecutive rows of $\mathbf{F}_N^H$, i.e., $\mathbf{F}_N^H = [\mathbf{F}_N^H(0),\mathbf{F}_N^H(1),\cdots,\mathbf{F}_N^H(Q-1)]^T$. By using the structure information of the upsampling matrix $\mathbf{U}_Q$, we have $(\mathbf{F}_N^H(l)\mathbf{U}_Q\mathbf{F}_M) = \frac{1}{\sqrt{Q}}\sum_{k=0}^{Q-1}\mathbf{F}_{M,k}^H(l)\mathbf{F}_M$, where $\mathbf{F}_{M,k}^H(l)$ is a sub-matrix of $\mathbf{F}_N^H(l)$ taking every M-th column of $\mathbf{F}_N^H(l)$, starting from the k-th column, i.e, taking the k-th, $(k+M)$-th, $\cdots$, $[k+(Q-1)M]$-th column of $\mathbf{F}_N^H(l)$. By using $\mathbf{F}_{M,k}^H(l) = \frac{1}{\sqrt{Q}}\mathbf{\Omega}_k(l)\mathbf{F}_M^H$, where $\mathbf{\Omega}_k(l)$ is a diagonal matrix with its i-th diagonal element being $e^{j\cdot 2\pi i(k+lM)/N}$, it is easy to obtain the i-th diagonal element of $\sum_{k=0}^{Q-1}\mathbf{F}_{M,k}^H(l)\mathbf{F}_M$ as

$$\sum_{k=0}^{Q-1} e^{j\cdot 2\pi i(k+lM)/N} = (1-e^{j\cdot i\epsilon_1})/(1-e^{j\cdot i\epsilon_2}) = \upsilon_l(i),$$

where $\epsilon_1 = 2\pi(Q+lM)/N$ and $\epsilon_2 = 2\pi(1+lM)/N$. Thus, we have $\mathbf{F}_N^H\mathbf{U}_Q\mathbf{F}_M = \mathbf{\Upsilon}$. Substituting into $\mathbf{H}_U$, we have (10). By using triangle equations, we obtain (14):

$$\begin{aligned}|\upsilon_l(i)|^2 =&|1-e^{j\cdot i\epsilon_1}|^2/|1-e^{j\cdot i\epsilon_2}|^2\\ =&[1-2\cos(i\epsilon_1)]/[1-2\cos(i\epsilon_2)]\\ =&[\sin(i\epsilon_1/2)]^2/[\sin(i\epsilon_2)/2]^2\end{aligned}$$

APPENDIX B
PROOF OF THEOREM 2

Firstly, by using $\mathbf{F}_N\mathbf{F}_N^H = \mathbf{I}_N$, we can write:

$$\mathbf{H}_D = (\mathbf{F}_M^H\mathbf{D}_Q\mathbf{F}_N)\cdot(\mathbf{F}_N^H\mathbf{\Phi}_\eta\mathbf{F}_N)\cdot(\mathbf{F}_N^H\mathbf{B}\mathbf{F}_N).$$

Similar to the proof to Theorem 1, we can easily achieve $\mathbf{H}_D = (\mathbf{F}_M^H\mathbf{D}_Q\mathbf{F}_N)\mathbf{J}^{(u)}\mathbf{H}_O$. Let us first split the N-point IDFT matrix $\mathbf{F}_N$ into Q equal size sub-matrices, each taking M consecutive columns of $\mathbf{F}_N^H$, i.e., $\mathbf{F}_N = [\mathbf{F}_N(0), \mathbf{F}_N(1), \cdots, \mathbf{F}_N(Q-1)]$. Note that the down sampling matrix $\mathbf{D}_Q$ multiplying with $\mathbf{F}_N(l)$ equals to an M-dimension DFT matrix $1/\sqrt{Q}\mathbf{F}_M$, thus, $\mathbf{F}_M^H\mathbf{D}_Q\mathbf{F}_N(l) = 1/\sqrt{Q}\mathbf{I}_M$. Substituting into $\mathbf{H}_D$ we can obtain (19).

APPENDIX C
PROOF OF (27) AND (28)

The desired signal at slice 1 can be written as

$$\mathbf{\Pi}_1(k) = \tilde{\mathbf{F}}_{N_{B1}}^H\mathbf{\Psi}_1^H\mathbf{R}_1\mathbf{A}_1^H\bar{\mathbf{B}}_1\mathbf{A}_1\mathbf{C}_1\mathbf{\Psi}_1\tilde{\mathbf{F}}_{N_{U1}}\mathbf{a}_1(k).$$

With sufficient CP length and well-designed filter, we can omit the ISI as discussed in Section IV-A. Then we can have

$$\begin{aligned}\mathbf{R}_1\mathbf{A}_1^H\bar{\mathbf{B}}_1\mathbf{A}_1\mathbf{C}_1 =&(\mathbf{R}_1\mathbf{A}_1^H\mathbf{C}_1)(\mathbf{R}_1\bar{\mathbf{B}}_1\mathbf{C}_1)(\mathbf{R}_1\mathbf{A}_1\mathbf{C}_1)\\ =&\mathbf{A}_{cir,1}^H\bar{\mathbf{B}}_{cir,1}\mathbf{A}_{cir,1},\end{aligned}$$

where $\mathbf{A}_{cir,1}^H$, $\bar{\mathbf{B}}_{cir,1}$ and $\mathbf{A}_{cir,1}$ are circular matrix of receiver filter, channel and transmitter filter, respectively. Hence, $\mathbf{\Pi}_1(k)$ can be written as

$$\begin{aligned}\mathbf{\Pi}_1(k)=&(\tilde{\mathbf{F}}_{N_{B1}}^H\mathbf{\Psi}_1^H\mathbf{A}_{cir,1}^H\mathbf{\Psi}_1\mathbf{F}_{N_{B1}})\cdot(\mathbf{F}_{N_{B1}}^H\mathbf{\Psi}_1^H\mathbf{B}_{cir,1}\mathbf{\Psi}_1\mathbf{F}_{N_{B1}})\\ &\cdot(\mathbf{F}_{N_{B1}}^H\mathbf{\Psi}_1^H\mathbf{A}_{cir,1}\mathbf{\Psi}_1\mathbf{F}_{N_{B1}})\cdot(\mathbf{F}_{N_{B1}}^H\tilde{\mathbf{F}}_{N_{U1}})\cdot\mathbf{a}_1(k)\\ =&1/\sqrt{Q}\mathbf{G}_1^H\mathbf{H}_1\mathbf{G}_1\mathbf{a}_1(k) = \mathbf{H}_{eff,1}\mathbf{a}_1(k)\end{aligned}$$

and thus we have equation (27).

For slice 2, following the same approach, the desired signal can be written as

$$\begin{aligned}\mathbf{\Pi}_2 =&\tilde{\mathbf{F}}_{N_{B2}}^H\mathbf{\Psi}_2^H\bar{\mathbf{R}}_2\mathbf{A}_2^H\bar{\mathbf{B}}_2\mathbf{A}_2\tilde{\mathbf{\Psi}}_2\mathbf{U}_Q\bar{\mathbf{C}}_2\mathbf{F}_{N_{U2}}\mathbf{a}_2\\ =&\mathbf{G}_2^H\mathbf{H}_2\mathbf{G}_2\tilde{\mathbf{F}}_{N_{N2}}^H\mathbf{U}_Q\mathbf{F}_{N_{U2}}\mathbf{a}_2.\end{aligned}$$

By using Theorem 1, we can have $\mathbf{F}_{N_{B2}}^H\mathbf{U}_Q\mathbf{F}_{N_{U2}} = 1/\sqrt{Q}\mathbf{\Upsilon}$. Hence, the desired signal at slice 2 can be achieved as $\mathbf{\Pi}_2 = \mathbf{H}_{eff,2}$, and thus equation (28) is obtained.

REFERENCES

[1] ITU-R M.2083-0, "IMT vision – framework and overall objectives of the future development of IMT for 2020 and beyond," Tech. Rep., Sept 2015.

[2] A. Ijaz *et al.*, "Enabling massive IoT in 5G and beyond systems: PHY radio frame design considerations," *IEEE Access*, vol. 4, pp. 3322–3339, 2016.

[3] M. Richart, J. Baliosian, J. Serrat, and J. L. Gorricho, "Resource slicing in virtual wireless networks: A survey," *IEEE Transactions on Network and Service Management*, vol. 13, no. 3, pp. 462–476, Sept 2016.

[4] C. Liang and F. R. Yu, "Wireless network virtualization: A survey, some research issues and challenges," *IEEE Communications Surveys Tutorials*, vol. 17, no. 1, pp. 358–380, Firstquarter 2015.

[5] Nokia, "Dynamic end-to-end network slicing for 5G," Tech. Rep., 2016.

[6] X. Foukas, G. Patounas, A. Elmokashfi, and M. K. Marina, "Network slicing in 5G: Survey and challenges," *IEEE Communications Magazine*, vol. 55, no. 5, pp. 94–100, May 2017.

[7] R. H. Wen, G. Feng, W. Tan, N. Rui, W. Cao, and S. Qin, "Protocol stack mapping of software defined protocol for next generation mobile networks," *IEEE Transaction on Mobile Computing*, pp. 1651–1665, Jul. 2018.

[8] L. Zhang, A. Ijaz, P. Xiao, A. Quddus, and R. Tafazolli, "Subband filtered multi-carrier systems for multi-service wireless communications," *IEEE Transactions on Wireless Communications*, vol. 16, no. 3, pp. 1893–1907, March 2017.

[9] A. Yazar and H. Arslan, "A flexibility metric and optimization methods for mixed numerologies in 5G and beyond," *IEEE Access*, vol. 6, pp. 3755–3764, 2018.

[10] 3GPP TR 36.802, "Narrowband internet of things (NB-IoT) – technical report for BS and UE radio transmission and reception (release 13)," Tech. Rep., June 2016.

[11] H. Ji, S. Park, J. Yeo, Y. Kim, J. Lee, and B. Shim, "Ultra-reliable and low-latency communications in 5G downlink: Physical layer aspects," *IEEE Wireless Communications*, vol. 25, no. 3, pp. 124–130, JUNE 2018.

[12] Y. P. E. Wang, X. Lin, A. Adhikary, A. Grovlen, Y. Sui, Y. Blankenship, J. Bergman, and H. S. Razaghi, "A primer on 3GPP narrowband internet of things," *IEEE Communications Magazine*, vol. 55, no. 3, pp. 117–123, March 2017.

[13] G. H. Golub and C. F. Van Loan, *Matrix Computations (3rd Ed.)*. Baltimore, MD, USA: Johns Hopkins University Press, 1996.

[14] A. Yazar and H. Arslan, "Flexible multi-numerology systems for 5G new radio," *Journal of Mobile Multimedia*, vol. 14, no. 4, pp. 367–394, 2018.

[15] J. Choi, B. Kim, K. Lee, and D. Hong, "A transceiver design for spectrum sharing in mixed numerology environments," *IEEE Transactions on Wireless Communications*, vol. 18, no. 5, pp. 2707–2721, May 2019.

[16] L. Zhang, A. Ijaz, P. Xiao, and R. Tafazolli, "Multi-service system: An enabler of flexible 5G air interface," *IEEE Communications Magazine*, vol. 55, no. 10, pp. 152–159, OCTOBER 2017.

[17] R1-166103, "Discussion on flexible frame structure with different numerologies," 3GPP TSG RAN1 Meeting #86, Tech. Rep., August 2016.

[18] A. B. Kihero, M. S. J. Solaija, and H. Arslan, "Multi-numerology multiplexing and inter-numerology interference analysis for 5G," *arXiv preprint arXiv:1905.12748*, 2019.

[19] B. Farhang-Boroujeny, "OFDM versus filter bank multicarrier," *IEEE Signal Processing Magazine*, vol. 28, no. 3, pp. 92–112, May 2011.

[20] G. Fettweis, M. Krondorf, and S. Bittner, "GFDM - generalized frequency division multiplexing," in *IEEE Vehicular Technology Conference*, April 2009, pp. 1–4.

[21] 5GNOW, "D3.2: 5G waveform candidate selection," Tech. Rep., 2014.

[22] Y. Chen, F. Schaich, and T. Wild, "Multiple access and waveforms for 5G: IDMA and universal filtered multi-carrier," in *IEEE Vehicular Technology Conference (VTC Spring)*, 2014, pp. 1–5.

[23] X. Zhang, M. Jia, L. Chen, J. Ma, and J. Qiu, "Filtered-OFDM - enabler for flexible waveform in the 5th generation cellular networks," in *2015 IEEE Global Communications Conference*, Dec 2015, pp. 1–6.

[24] X. Zhang, L. Zhang, P. Xiao, D. Ma, J. Wei, and Y. Xin, "Mixed numerologies interference analysis and inter-numerology interference cancellation for windowed OFDM systems," *IEEE Transactions on Vehicular Technology*, vol. 67, no. 8, pp. 7047–7061, Aug 2018.

[25] P. Guan, D. Wu, T. Tian, J. Zhou, X. Zhang, L. Gu, A. Benjebbour, M. Iwabuchi, and Y. Kishiyama, "5G field trials: OFDM-based waveforms and mixed numerologies," *IEEE Journal on Selected Areas in Communications*, vol. 35, no. 6, pp. 1234–1243, June 2017.

[26] H. Chen, J. Hua, F. Li, F. Chen, and D. Wang, "Interference analysis in the asynchronous f-ofdm systems," *IEEE Transactions on Communications*, vol. 67, no. 5, pp. 3580–3596, May 2019.

[27] O. Sallent, J. Perez-Romero, R. Ferrus, and R. Agusti, "On radio access network slicing from a radio resource management perspective," *IEEE Wireless Communications*, vol. PP, no. 99, pp. 2–10, 2017.

[28] V. F. Monteiro, M. Ericson, and F. R. P. Cavalcanti, "Fast-RAT scheduling in a 5G multi-RAT scenario," *IEEE Communications Magazine*, vol. 55, no. 6, pp. 79–85, 2017.

[29] A. Yazar and H. Arslan, "Reliability enhancement in multi-numerology-based 5G new radio using ini-aware scheduling," *EURASIP Journal on Wireless Communications and Networking*, vol. 2019, no. 1, p. 110, 2019.

[30] H. Lin, "Flexible configured OFDM for 5G air interface," *IEEE Access*, vol. 3, pp. 1861–1870, 2015.

[31] M. Fuhrwerk, J. Peissig, and M. Schellmann, "On the design of an fbmc based air interface enabling channel adaptive pulse shaping per sub-band," in *2015 23rd European Signal Processing Conference (EUSIPCO)*, Aug 2015, pp. 384–388.

[32] R1-161981, "NB-PSS and NB-SSS design," 3GPP TSG RAN WG1 NB-IoT Ad-Hoc Meeting, Tech. Rep., 2016.

[33] L. Zhang, A. Ijaz, P. Xiao, and R. Tafazolli, "Channel equalization and interference analysis for uplink narrowband internet of things (NB-IoT)," *IEEE Communications Letters*, vol. PP, no. 99, pp. 1–1, 2017.